J. Fluid Mech. (2013), *vol.* 736, *pp.* 316–350. © Cambridge University Press 2013
doi:10.1017/jfm.2013.494

Generalized phase average with applications to sensor-based flow estimation of the wall-mounted square cylinder wake

J. A. Bourgeois[1], B. R. Noack[2] and R. J. Martinuzzi[1],†

[1]Department of Mechanical and Manufacturing Engineering, Schulich School of Engineering, University of Calgary, 2500 University Drive NW, Calgary, AB, T2N 1N4, Canada

[2]Institut PPRIME, CNRS - Université de Poitiers - ENSMA, UPR 3346, Département Fluides, Thermique, Combustion, CEAT, 43 rue de l'Aérodrome, F-86036 POITIERS CEDEX, France

(Received 21 August 2012; revised 20 June 2013; accepted 15 September 2013; first published online 6 November 2013)

We experimentally investigate the three-dimensional wake behind a finite wall-mounted square cylinder at $Re = 12\,000$ and aspect ratio of 4. Focus is placed on the base flow and oscillatory fluctuation. Time-resolved three-dimensional velocity fields are constructed from high-frame-rate particle image velocimetry (PIV) and simultaneously recorded surface pressure measurements. All three velocity components are resolved in a rectangular near-wake region by two orthogonal dense arrays of parallel PIV planes. A key enabler is a generalized phase average incorporating a slowly varying base flow, a variable oscillation amplitude and higher harmonics. These generalizations reduce the instantaneous residual 30 % below those of a traditional phase average. Moreover, the resolved variations reveal analytical constraints of the mean flow and oscillation levels, such as the mean-field paraboloid. The proposed methodology for generalized phase averaging and for construction of three-dimensional velocity fields from two-dimensional PIV data is applicable to a large class of turbulent flows with oscillatory dynamics.

Key words: low-dimensional models, jets, wakes

1. Introduction

A large class of turbulent flows exhibit dominant oscillatory dynamics. Examples include vortex shedding behind obstacles (Williamson 1996), Kelvin–Helmholtz vortices in mixing layers (Liu 1989), Rossiter modes in cavities (Rowley & Williams 2006) and wavy structures in Taylor–Couette flow, just to name a few. These flows generally share dominant oscillatory structures with low-frequency drifts of the base flow and a low-frequency modulation of the fluctuation level.

In this study, we propose a methodology to extract these coherent structures from experimental two-dimensional particle image velocimetry (PIV) data and construct time-resolved three-dimensional velocity fields. The first step is to filter two-dimensional velocity fields within a quantitative coherent structure description comprising few parameters. The second step is to combine two-dimensional

† Email address for correspondence: rmartinu@ucalgary.ca

https://doi.org/10.1017/jfm.2013.494 Published online by Cambridge University Press

uncorrelated PIV snapshots into three-dimensional time-resolved flows via a correlation with time-resolving pressure sensors.

Since Leonardo da Vinci's drawings of flows, coherent structures have been characterized by vortices or vortex skeletons (Lugt 1995). Modern versions include snapshot topology (Perry & Chong 1987) and generalizations for time-varying flows (Haller 2001, 2005; Kasten *et al.* 2012*a*,*b*). This Lagrangian flow description marks local pronounced flow features, but lacks convenient quantitative global velocity field parametrization. An Eulerian alternative is the Galerkin expansion of the velocity field $\boldsymbol{u}$ into a base flow $\boldsymbol{u}_0$ and a sum of N space-dependent modes $\boldsymbol{u}_i$, $i = 1, \ldots, N$ with corresponding time-dependent mode amplitudes a_i (cf. Fletcher 1984),

$$\boldsymbol{u}(\boldsymbol{x}, t) = \boldsymbol{u}_0(\boldsymbol{x}) + \sum_{i=1}^{N} a_i(t)\boldsymbol{u}_i(\boldsymbol{x}). \tag{1.1}$$

A myriad of modal decompositions are in use, from mathematical expansions guaranteeing completeness, physical expansions incorporating stability and other properties of the Navier–Stokes equation, to empirical decompositions from available flow data. In this study, we focus on the latter category. Here, examples include the proper orthogonal decomposition (POD) minimizing the mean resolution residual (Holmes *et al.* 2012), the dynamic mode decomposition (DMD) or Koopman modes (Rowley *et al.* 2009; Schmid 2010) and numerous generalizations for transients of multiple operating conditions. Some generalizations incorporate the correlation between flow and sensors (or other observables) such as the extended POD (Borée 2003) and the observable inferred decomposition (OID) (Schlegel *et al.* 2012).

The above expansions can be considered a generalization or realization of the triple decomposition of the flow $\boldsymbol{u}$ into a slowly varying base flow $\boldsymbol{u}_B$, a low-dimensional, large-scale coherent structure contribution $\boldsymbol{u}_C$ and a stochastic, small-scale turbulent fluctuation $\boldsymbol{u}_S$ (Reynolds & Hussain 1972),

$$\boldsymbol{u} = \boldsymbol{u}_B + \boldsymbol{u}_C + \boldsymbol{u}_S. \tag{1.2}$$

Here, $\boldsymbol{u}_B$ corresponds to $\boldsymbol{u}_0$ in the Galerkin expansion, $\boldsymbol{u}_C$ to the expansion and $\boldsymbol{u}_S$ to the neglected residual. The simplest realization of the triple decomposition is the phase average, where $\boldsymbol{u}_C$ is parametrized by a single phase. The phase may be imposed by external forcing or may arise from an intrinsic clockwork of vortex shedding. In this study, we generalize phase averaging to include low-frequency drifts in the base flow, variations in the oscillation level as well as higher harmonics. This generalization includes the expansion of the minimal Galerkin model with a shift mode for base flow variation and an oscillatory mode pair (Noack *et al.* 2003; Tadmor *et al.* 2010).

The second task is the construction of three-dimensional flows from two-dimensional PIV data along orthogonal planes. For some flows, such as the swirling jet, symmetries of the coherent structures may be exploited towards this goal (Oberleithner *et al.* 2011). A more general alternative is the use of sensors and correlation between the flow (PIV) and these sensors (Adrian 1998; Taylor & Glauser 2004). This alternative is pursued in this study.

Our methodology is exemplified for the turbulent vortex shedding behind a wall-mounted square cylinder of finite height. This flow is a well-established benchmark configuration for oscillatory coherent structures with pronounced three-dimensional features. It is characterized by the nearly periodic shedding of vortices from the opposing vertical obstacle lateral faces. These shed structures deform quickly in the wake and mainly streamwise-oriented vorticity strands connect successive

https://doi.org/10.1017/jfm.2013.494 Published online by Cambridge University Press

counter-rotating vortices, giving rise to a train of half-loop structures (Bourgeois, Sattari & Martinuzzi 2011). From a fundamental perspective, the interaction between the principal shed vortices and connector strands gives rise to highly modulated velocity and pressure fluctuations which are not adequately described using traditional phase averaging techniques (cf. Sattari, Bourgeois & Martinuzzi 2012). A better understanding of these interactions, however, is of significant practical consequence. These modulations are intimately related to high structural loading on the generating obstacle and are a major source of downstream interference. Of perhaps greater importance are the associated downburst phenomena in the wake, which can enhance mixing but can also transport contaminants from chimney stacks or debris from buildings, posing discomfort or even danger to pedestrian traffic in the wake of free-standing structures.

The paper is organized as follows: the experimental set-up is described in §§ 2 and 3 provides the analytical framework and methodology for determining the generalized phase average. In § 4, the technique for global flow estimation based on surface pressure measurements is presented. These techniques are then applied to the analysis of the wall-mounted bluff-body wake. Section 5 presents the results of the generalized phase average. In § 6, the three-dimensional flow estimation of the wake is discussed and we propose a six-dimensional least-order model for the base flow, fundamental harmonics and stochastic fluctuations (details are found in appendix A). A summary and outlook conclude the paper (§ 7).

2. Experimental facility

Experiments were conducted in an open working section suction wind tunnel facility, shown in figure 1. Still air is drawn through a 3 m diameter inlet and passes through three 20 mesh metal grids, a 24 and a 30 mesh metal grid, and one 80 mesh nylon screen. It enters the working section through a 36:1 inlet-area contraction ratio nozzle. The working section of the tunnel is open with a 0.5 m jet providing a nominally uniform stream in which an aluminium sharp-leading-edge flat plate (1.20 m $\times$ 0.80 m $\times$ 0.01 m) is mounted, providing a base turbulent boundary layer flow within which a finite square-cross-section cylinder is placed (aspect ratio, $h/d = 4$, where $d = 0.0127$ m and $h = 0.0508$ m).

The coordinate system origin is centred along the axis of the obstacle with $z = 0$ at the plate junction. While dimensional quantities are provided in this section for the description of the facility, throughout the remainder of the manuscript, all quantities provided are non-dimensionalized by the scaling length d, time scale d/U_∞, and the density, ρ.

The free-stream conditions of the flow correspond to a mean velocity of $U_\infty = 15$ m s^{-1}, a turbulence intensity level of 0.8 %, and a Reynolds number of $Re = U_\infty d/\nu = 12\,000$. The cylinder is mounted at $x = 200$ mm ($\approx 16d$) from the leading edge of the plate where the boundary-layer thickness (in the absence of the obstacle) is $\delta/d = 0.72$. Figure 2 shows profiles of the mean and root-mean-square (r.m.s.) velocity measured using hot-wire anemometry. It was verified that the boundary layer did not vary in the spanwise direction at least within the range $-12 < y/d < 12$.

The chosen configuration is a well-investigated benchmark of a wake behind finite wall-mounted cylinders. A parametric study in terms of the Reynolds number and aspect ratios has been performed by Wang *et al.* (2006) and Wang & Zhou (2009).

https://doi.org/10.1017/jfm.2013.494 Published online by Cambridge University Press

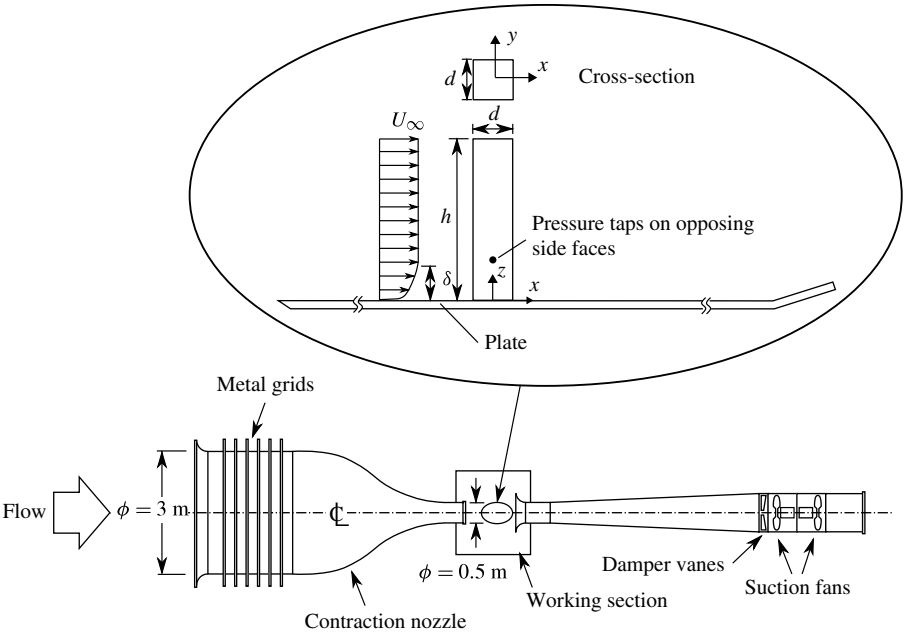


FIGURE 1. Wind tunnel facility with working section close-up.

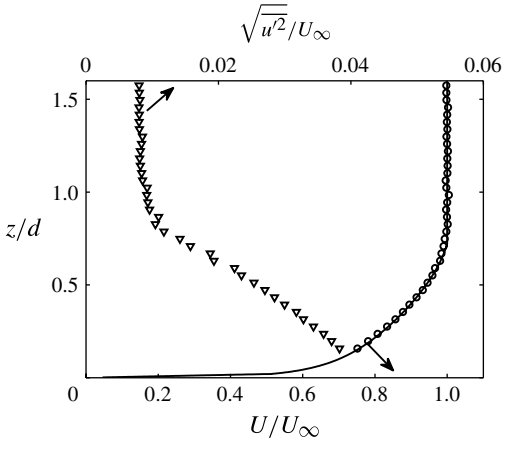


FIGURE 2. Boundary-layer mean and r.m.s. velocity profiles at $x = 0$ (without cylinder), $16d$ downstream of the plate leading edge.

The hot-wire anemometry was carried out with a single TSI 1210-20 hot-wire anemometry probe at a sampling rate of 10.24 kHz with a TSI IFA-100 bridge and a 5 kHz anti-aliasing low-pass filter. Spectra were computed 10 times over 10 s windows and averaged. The Strouhal number was found to be $St = f_s d/U_\infty = 0.100 \pm 0.003$ where the vortex-shedding frequency was $f_s \approx 120$ Hz.

The locations of the planes measured in the present study are shown schematically in figure 3. The PIV planes spanned a field of view of approximately $12d \times 12d$. A

https://doi.org/10.1017/jfm.2013.494 Published online by Cambridge University Press

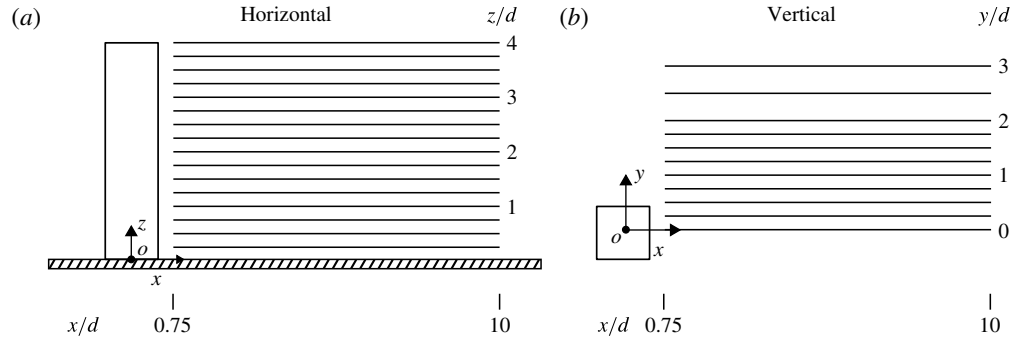


FIGURE 3. Schematic showing positions of PIV planes as lines. The horizontal (x–y) planes are shown on the left and the vertical (x–z) planes are shown on the right.

spacing of $d/4$ was typically taken between planes (with the exception of x–z planes with $y/d > 2$ where the spacing was $d/2$).

The PIV system used was a high-frame-rate LaVision FlowMaster system with a Photonics Industries 527 nm Nd:YLF laser used to produce a light sheet of aperture angle 12° and a HighSpeedStar 5 CMOS camera (1024×1024 pixels). The system was operated in a double-pulse mode with a 50 μs pulse separation between image pairs, which were typically captured at 500 Hz, corresponding to more than 4 data points per vortex-shedding cycle. For each measurement plane, 5000–10 000 image pairs were captured, providing statistics over 1200–2300 vortex-shedding cycles. Interrogation windows of 32×32 pixels or, when more resolution was desired, 16×16 pixels were used in a frame straddled arrangement, providing resolution of $d/4$ or $d/8$, respectively. Olive oil seeding particles of roughly 1 μm were generated with a Laskin nozzle seed generator. This configuration provides an estimated uncertainty (Westerweel 2000) on individual vector measurements of $\Delta u/U_\infty = \pm 0.025$.

A TTL signal from the PIV system synchronized velocity and surface pressure measurements on opposing sides of the obstacle at $z/h = 0.25$. The pressure was sampled at 10.24 kHz. The higher sampling rate was desired to accurately determine the instantaneous phase and amplitude of the fluctuating pressure signal. The pressure tap-tube-sensor assembly had a flat frequency response up to roughly 250 Hz.

For global flow estimation, the flow in each PIV plane is estimated using a parameterization in terms of measured surface pressure values. Trilinear interpolation of the planar data has been undertaken onto a volumetric grid with step size $d/8$.

3. Generalized phase average

We commence with the triple decomposition (Reynolds & Hussain 1972) of the velocity field into a base flow as well as coherent and stochastic fluctuations (§ 3.1). In §§ 3.2–3.4 the computation of these contributions is outlined.

3.1. *Triple decomposition*

The starting point of the proposed low-order flow description is the triple decomposition of Reynolds & Hussain (1972). Accordingly, the velocity field is decomposed in a base flow $\boldsymbol{u}_B$ and fluctuation $\boldsymbol{u}'$. As refinement, the fluctuation is further decomposed into a coherent and stochastic contribution, $\boldsymbol{u}_\phi$ and $\boldsymbol{u}_S$,

https://doi.org/10.1017/jfm.2013.494 Published online by Cambridge University Press

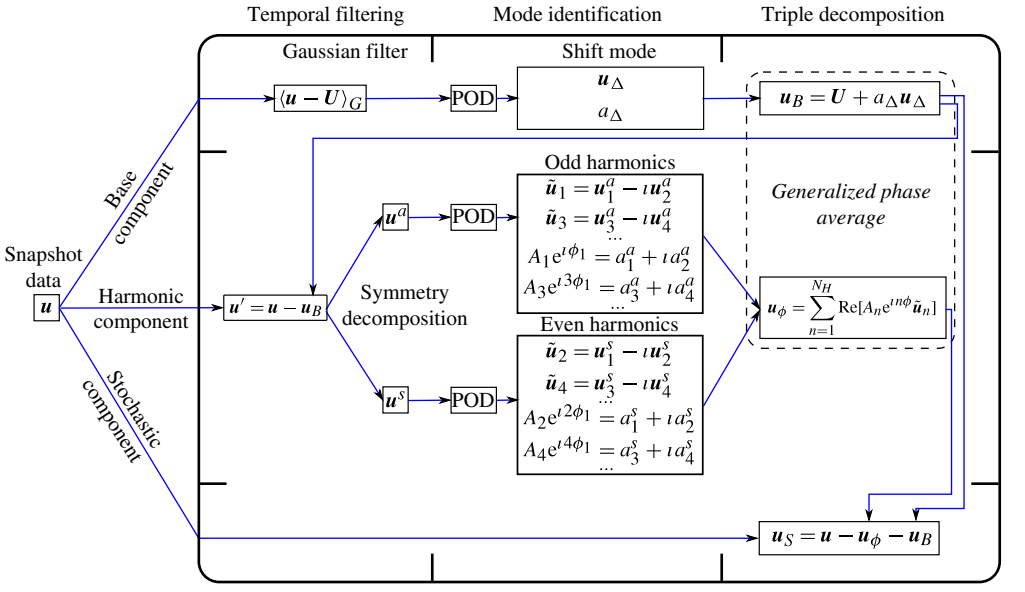


FIGURE 4. (Colour online) Flow chart illustrating data reduction procedure to identify generalized phase average from a set of velocity field snapshots. The generalization comprises the time-varying amplitudes $(a_\Delta, A_1, \ldots, A_n)$ and the higher harmonics.

respectively:

$$\boldsymbol{u}(\boldsymbol{x}, t) = \boldsymbol{u}_B(\boldsymbol{x}, t) + \boldsymbol{u}'(\boldsymbol{x}, t) \tag{3.1a}$$

$$\boldsymbol{u}'(\boldsymbol{x}, t) = \boldsymbol{u}_\phi(\boldsymbol{x}, t) + \boldsymbol{u}_S(\boldsymbol{x}, t). \tag{3.1b}$$

In general, the base flow $\boldsymbol{u}_B$ is taken as the time or ensemble mean or as the slowly varying component. The coherent contribution $\boldsymbol{u}_\phi$ is considered a footprint of low-dimensional coherent structures. Interpretations range from phase averages with constant amplitude (Perrin *et al.* 2006) via a truncated POD (Holmes *et al.* 2012) to the residual of uncorrelated noise (Farge *et al.* 2003). In this wake study, we generalize phase averaging by allowing for slow variations of the base flow and of the oscillation level following Dušek, Le Gal & Fraunié (1994) and Tadmor *et al.* (2011). The residual of $\boldsymbol{u}_S := \boldsymbol{u} - \boldsymbol{u}_B - \boldsymbol{u}_\phi$ is considered as a high-dimensional small-scale stochastic component. The corresponding decompositions of the Navier–Stokes equation can be found in the original paper by Reynolds & Hussain (1972) for time-averaged base flows and in alternative versions of the authors (Luchtenburg *et al.* 2009; Noack *et al.* 2010; Tadmor *et al.* 2010).

The proposed decomposition approach consists of three steps (see the overview in figure 4). For reasons of simplicity, these steps are sketched for PIV data of the x, y parallel plane. First, the base flow is obtained from Gaussian filtered original data. Second, the considered harmonics of the residual are inferred using the POD and symmetry properties of the flow. Finally, the residual of the extracted base flow and oscillatory component is considered as the stochastic contribution. The details will be explained in the subsequent §§ 3.2–3.4.

https://doi.org/10.1017/jfm.2013.494 Published online by Cambridge University Press

3.2. *Base flow* $\boldsymbol{u}_B$

First, the velocity data is Gaussian filtered to provide a short-time average of the velocity field data. Thus, $\boldsymbol{u}_B$ resolves mean field variations with time scales which are long relative to an oscillation period,

$$\langle \boldsymbol{u}(\boldsymbol{x}, t) - \boldsymbol{U}(\boldsymbol{x}) \rangle_G = \int_{-\infty}^{\infty} (\boldsymbol{u}(\boldsymbol{x}, \tau) - \boldsymbol{U}(\boldsymbol{x})) g(\tau - t)\, \mathrm{d}\tau \tag{3.2}$$

$$g(t) = \frac{1}{\sqrt{2\pi}\sigma_b} \mathrm{e}^{-t^2/2\sigma_b^2}. \tag{3.3}$$

Here, σ_b is the bandwidth of the Gaussian kernel which is chosen to be the same for velocity and pressure data (see § 4.2). Following Tadmor *et al.* (2010), the resulting base flow $\boldsymbol{u}_B$ is approximated by a first-order POD decomposition comprising the time-average $\boldsymbol{U}$ and the shift mode $\boldsymbol{u}_\Delta$ as first (most energetic) POD mode,

$$\boldsymbol{u}_B(\boldsymbol{x}, t) = \boldsymbol{U}(\boldsymbol{x}) + a_\Delta(t)\boldsymbol{u}_\Delta(\boldsymbol{x}). \tag{3.4}$$

3.3. *Oscillatory fluctuation* $\boldsymbol{u}_\phi$

The oscillatory component $\boldsymbol{u}_\phi$ is extracted from fluctuation (3.1*a*), more precisely from a POD with respect to the standard inner product

$$(\boldsymbol{v}, \boldsymbol{w})_\Omega = \int_\Omega \boldsymbol{v} \cdot \boldsymbol{w}\, \mathrm{d}\boldsymbol{x} \tag{3.5}$$

of the observation domain Ω with its area/volume elements $\mathrm{d}\boldsymbol{x}$. The corresponding norm is defined by $\|\boldsymbol{v}\|_\Omega = \sqrt{(\boldsymbol{v}, \boldsymbol{v})_\Omega}$.

The POD modes of wakes behind circular or square cylinders can be shown to be either symmetric or antisymmetric with respect to the plane $y = 0$, owing to symmetry of the two-point cross-correlation (Deane *et al.* 1991). Following Holmes *et al.* (2012), such symmetries of the flow should be exploited whenever possible in preprocessing the data. Exploiting these symmetries effectively acts as a prefilter reinforcing known properties of the modes relative to random contributions, thus reducing error propagation and thereby increasing statistical convergence rates with respect to the number of employed snapshots. Hence, the velocity fluctuation is decomposed into a symmetric $\boldsymbol{u}^s$ and antisymmetric part $\boldsymbol{u}^a$ with respect to the x–z plane,

$$\boldsymbol{u}'(\boldsymbol{x}, t) = \boldsymbol{u}^s(\boldsymbol{x}, t) + \boldsymbol{u}^a(\boldsymbol{x}, t), \tag{3.6}$$

where the components of the symmetric velocity field are defined by

$$u^s(x, y, z, t) = \tfrac{1}{2}[u(x, y, z, t) + u(x, -y, z, t)] \tag{3.7a}$$

$$v^s(x, y, z, t) = \tfrac{1}{2}[v(x, y, z, t) - v(x, -y, z, t)] \tag{3.7b}$$

$$w^s(x, y, z, t) = \tfrac{1}{2}[w(x, y, z, t) + w(x, -y, z, t)] \tag{3.7c}$$

and the components of the antisymmetric velocity field read

$$u^a(x, y, z, t) = \tfrac{1}{2}[u(x, y, z, t) - u(x, -y, z, t)] \tag{3.8a}$$

$$v^a(x, y, z, t) = \tfrac{1}{2}[v(x, y, z, t) + v(x, -y, z, t)] \tag{3.8b}$$

$$w^a(x, y, z, t) = \tfrac{1}{2}[w(x, y, z, t) - w(x, -y, z, t)]. \tag{3.8c}$$

https://doi.org/10.1017/jfm.2013.494 Published online by Cambridge University Press

In both contributions, the v velocity component has opposite symmetry properties with respect to the u, w components. In addition, the symmetric and antisymmetric vector fields are orthogonal to each other in terms of the inner product (3.5).

Throughout the remaining manuscript, the superscripts 'a' and 's' will be used to identify antisymmetric and symmetric modes and mode amplitudes.

The harmonic modes are extracted from a POD expansion of the symmetric and antisymmetric components of the velocity fluctuation, i.e.

$$\boldsymbol{u}'(\boldsymbol{x}, t) = \boldsymbol{u}(\boldsymbol{x}, t) - \boldsymbol{u}_B(\boldsymbol{x}, t) = \boldsymbol{u}^s(\boldsymbol{x}, t) + \boldsymbol{u}^a(\boldsymbol{x}, t) \tag{3.9}$$

where

$$\boldsymbol{u}^s(\boldsymbol{x}, t) = \sum_{i=1}^{N_s} a_i^s(t)\boldsymbol{u}_i^s(\boldsymbol{x}) \tag{3.10a}$$

$$\boldsymbol{u}^a(\boldsymbol{x}, t) = \sum_{i=1}^{N_a} a_i^a(t)\boldsymbol{u}_i^a(\boldsymbol{x}). \tag{3.10b}$$

Here, $\boldsymbol{u}_i^{s,a}(\boldsymbol{x})$ denote the POD modes, $a_i^{s,a}(t)$ denote the mode amplitudes and $N_{s,a}$ denote the order of the expansion. The symmetric/antisymmetric flow field decomposition is performed for all planes with statistical symmetries. In this study, these domains are x, y parallel PIV regions which are symmetrically located with respect to the $y = 0$ plane.

The orthogonality of the symmetric and antisymmetric components implies a corresponding additivity of the turbulent kinetic energy (TKE):

$$K = \frac{1}{2}\int_\Omega \boldsymbol{u}' \cdot \boldsymbol{u}' \,\mathrm{d}V = \underbrace{\frac{1}{2}\int_\Omega \boldsymbol{u}^s \cdot \boldsymbol{u}^s \,\mathrm{d}V}_{K^s} + \underbrace{\frac{1}{2}\int_\Omega \boldsymbol{u}^a \cdot \boldsymbol{u}^a \,\mathrm{d}V}_{K^a}. \tag{3.11}$$

The symmetric and antisymmetric contribution to the TKE can be estimated from the symmetric and antisymmetric POD eigenvalues, λ_i^s and λ_i^a, respectively:

$$K^s = \frac{1}{2}\sum_{i=1}^{N_s} \lambda_i^s, \tag{3.12a}$$

$$K^a = \frac{1}{2}\sum_{i=1}^{N_a} \lambda_i^a. \tag{3.12b}$$

In the final step, we exploit the common observation of the POD modes of periodic wakes with symmetry with respect to $y = 0$ (Deane *et al.* 1991; Noack *et al.* 2003). They form pairs representing antisymmetric odd and symmetric even harmonics. For turbulent wakes, this symmetry property cannot be taken for granted but must be validated when applied.

The first two POD modes can be lumped into a single complex mode

$$\tilde{\boldsymbol{u}}_1(\boldsymbol{x}) = \boldsymbol{u}_1^a(\boldsymbol{x}) - \imath\boldsymbol{u}_2^a(\boldsymbol{x}) \tag{3.13}$$

with the complex amplitude

$$A_1(t)\mathrm{e}^{\imath\phi_1(t)} = a_1^a(t) + \imath a_2^a(t). \tag{3.14}$$

https://doi.org/10.1017/jfm.2013.494 Published online by Cambridge University Press

Here, $\imath = \sqrt{-1}$ represents the imaginary unit. The modulus A_1 and phase ϕ_1 are the polar coordinates of (a_1, a_2).

$$A_1(t) = \sqrt{a_1^a(t)^2 + a_2^a(t)^2} \tag{3.15a}$$

$$\phi_1(t) = \tan^{-1}\left(\frac{a_2^a(t)}{a_1^a(t)}\right). \tag{3.15b}$$

Now, the first harmonic reads

$$a_1^a(t)\boldsymbol{u}_1^a(\boldsymbol{x}) + a_2^a(t)\boldsymbol{u}_2^a(\boldsymbol{x}) = \mathrm{Re}[A_1(t)\mathrm{e}^{\imath\phi_1(t)}\tilde{\boldsymbol{u}}_1(\boldsymbol{x})], \tag{3.16}$$

where $\mathrm{Re}[\cdot]$ denotes the real part of the complex vector field.

In general, the nth odd or even harmonic can similarly be represented as, respectively,

$$\tilde{\boldsymbol{u}}_{2n-1}(\boldsymbol{x}) = \boldsymbol{u}_{2n-1}^a(\boldsymbol{x}) - i\boldsymbol{u}_{2n}^a(\boldsymbol{x}) \tag{3.17a}$$

$$\tilde{\boldsymbol{u}}_{2n}(\boldsymbol{x}) = \boldsymbol{u}_{2n-1}^s(\boldsymbol{x}) - i\boldsymbol{u}_{2n}^s(\boldsymbol{x}). \tag{3.17b}$$

The odd harmonic with index $2n-1$ can similarly be represented by the antisymmetric components

$$A_{2n-1}(t)\mathrm{e}^{\imath(2n-1)\phi_1(t)} = a_{2n-1}^a(t) + \imath a_{2n}^a(t) \tag{3.18}$$

while each even harmonic with index $2n$ can be represented by the symmetric components

$$A_{2n}(t)\mathrm{e}^{\imath 2n\phi_1(t)} = a_{2n-1}^s(t) + \imath a_{2n}^s(t). \tag{3.19}$$

It should be noted that the phase ϕ_1 of the first harmonics defines the phases of the higher harmonics. Otherwise, we would have independent oscillations.

Generalizing (3.16), the oscillatory fluctuation is approximated by the first N_H harmonics

$$\boldsymbol{u}_\phi(\boldsymbol{x}, \phi_1(t), A_n(t)) = \sum_{n=1}^{N_H} \mathrm{Re}[A_n(t)\mathrm{e}^{\imath n\phi_1(t)}\tilde{\boldsymbol{u}}_n(\boldsymbol{x})]. \tag{3.20}$$

Here, A_n is the amplitude of harmonic component n, $\phi_n = n\phi_1$ is its phase and $\tilde{\boldsymbol{u}}_n(\boldsymbol{x})$ is the complex mode.

3.4. *Stochastic fluctuation* $\boldsymbol{u}_S$

The stochastic term, $\boldsymbol{u}_S$, is the unresolved residual of the decomposition, $\boldsymbol{u}_S = \boldsymbol{u} - \boldsymbol{u}_B - \boldsymbol{u}_\phi$ from (3.1). For dynamic models, the stochastic term plays an important role as energy sink for the oscillatory fluctuation and in the Reynolds stress term for the mean flow.

The aforementioned approach and procedure is general and directly applicable to three-dimensional resolved fields obtained either by numerical simulations or experimental measurements. The next section addresses the dynamically consistent construction of a time-resolved three-dimensional field from uncorrelated planar measurements.

4. Estimation of the time-resolved three-dimensional wake

In this section, the estimation of the time-resolved three-dimensional wake is outlined, in the spirit of the three-dimensional swirling jet reconstruction of

https://doi.org/10.1017/jfm.2013.494 Published online by Cambridge University Press

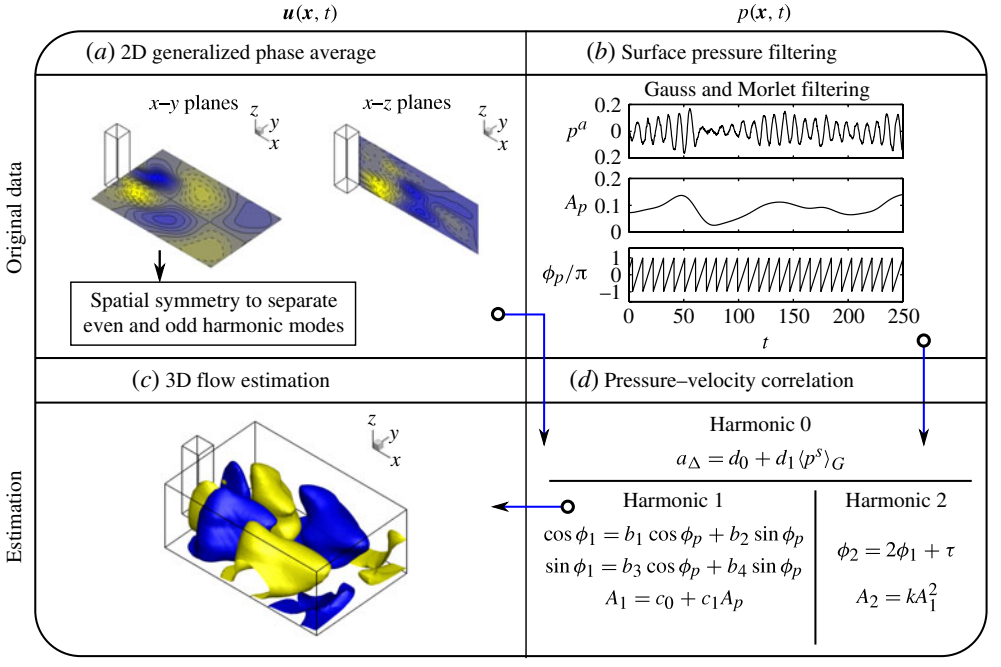


FIGURE 5. (Colour online) Flow chart illustrating the global three-dimensional flow estimation. The data reduction proceeds by (*a*) conducting local planar POD of PIV planes in parallel with (*b*) processing the surface pressure data, (*c*) relating local planar phase, amplitude and shift mode velocity state with the state of the pressure, and (*d*) estimating global velocity field snapshots based on a pressure signal and performing the POD to obtain global modes.

uncorrelated two-dimensional PIV snapshots in Oberleithner *et al.* (2011). The generalized phase average in the *x*–*y* planes and *x*–*z* planes (§ 4.1) is employed as a filter for time-resolved three-dimensional flow construction from pressure sensors on the cylinder surface (§ 4.2). The PIV snapshots are recorded simultaneously with the pressure signals. The pressure is sampled at 10.24 kHz, or approximately 50 times the PIV sampling rate, to ensure good phase resolution. Thus, a correlation with the PIV and pressure readings is established. In (§ 4.3), the amplitudes and phases of the pressure and velocity field are linearly linked. This correlation allows one to link each pressure reading to any given two-dimensional PIV planes from which a three-dimensional velocity field may be constructed. Thus, time-resolved pressure readings yield a three-dimensional time-dependent velocity field.

Figure 3 shows the corresponding *x*–*y* planes with u, v components and *x*–*z* planes with u, w components. Finally, the global velocity field is computed by trilinear interpolation of the PIV data onto a grid of the domain $(x, y, z) \in [0.75, 10] \times [-3, 3] \times [0.25, 4]$. The corresponding methodology is outlined in figure 5 and detailed in the following sections.

4.1. *x–y and x–z PIV planes*

The *x*–*y* PIV planar data are processed as per figure 4. Only the in-plane velocity components (u, v) are available, and the POD modes and their amplitudes are found over the plane $(x, y) \in [0.75, 10] \times [-3, 3]$.

https://doi.org/10.1017/jfm.2013.494 Published online by Cambridge University Press

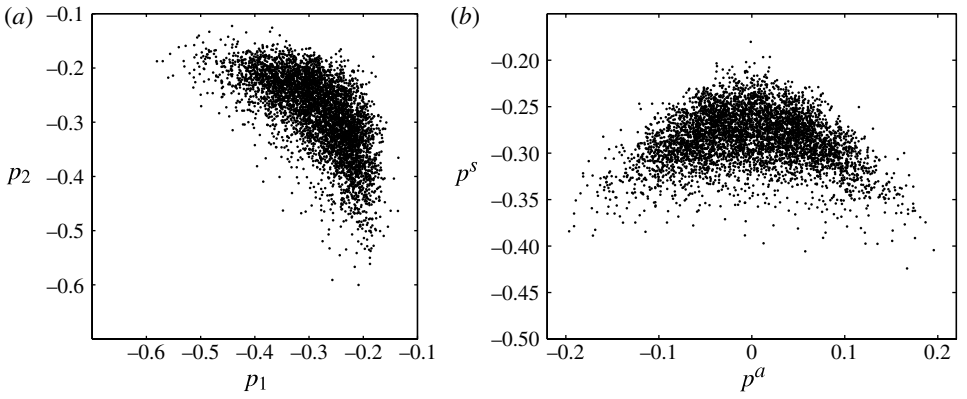


FIGURE 6. Scatter plot of pressure data on opposing sides of the obstacle (a) and the symmetric and antisymmetric pressure (b). The parabolic envelope of the right-hand side figure foreshadows mean field relations explained later in the text.

The processing of the x–z PIV data follows the same methodology of the x–y planes described above without the separation of symmetric and antisymmetric components. Data are only obtained on one side of $y = 0$. Therefore, the determination of the instantaneous symmetric and antisymmetric contributions of the field is not possible. Only the in-plane velocity components (u, w) are available, and the POD is found over the plane $(x, z) \in [0.75, 10] \times [0.25, 4]$.

When the three-dimensional flow field is constructed, information concerning the x–z planes for $y < 0$ needs to be added. This was achieved by imposing the discussed symmetries of the previous section on the constructed three-dimensional POD modes.

4.2. *Pressure state reference sensors*

Surface pressure measurements on the body are used as reference sensors for the state estimate of the wake flow. The pressure field in the flow and on the surface may be split into symmetric and antisymmetric parts

$$p(\boldsymbol{x}, t) = p^s(\boldsymbol{x}, t) + p^a(\boldsymbol{x}, t), \tag{4.1a}$$

$$p^s(x, y, z, t) = \tfrac{1}{2}[p(x, y, z, t) + p(x, -y, z, t)], \tag{4.1b}$$

$$p^a(x, y, z, t) = \tfrac{1}{2}[p(x, y, z, t) - p(x, -y, z, t)]. \tag{4.1c}$$

In the present study, only two pressure sensors have been used, positioned symmetrically about $y = 0$ on opposing side faces of the obstacle. Any reference to the spatial position will therefore be dropped such that the symmetric and antisymmetric pressure will be understood as $p^s = (p_1 + p_2)/2$ and $p^a = (p_1 - p_2)/2$ where p_1 and p_2 are the pressure measurements on either side of the obstacle. Figure 6 shows a scatter plot of p_1 and p_2 juxtaposed against p^s and p^a.

A linear pressure–velocity correlation is assumed following Noack, Papas & Monkewitz (2005) and Noack (2006) and many others. The antisymmetric pressure will be linked to the antisymmetric velocity fluctuation, in particular the dominant first harmonics, while the low-pass filtered symmetric pressure correlates with the shift mode of the base flow variation.

The antisymmetric part is filtered using a complex continuous wavelet transform, W, where the filtered signal is represented as a modulated sinusoid. Here, phase and

https://doi.org/10.1017/jfm.2013.494 Published online by Cambridge University Press

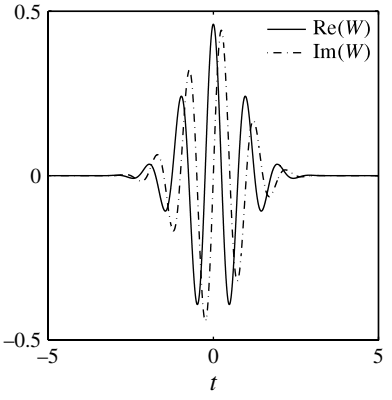


FIGURE 7. Morlet wavelet.

amplitude are taken from the wavelet transform. We employ a complex Morlet wavelet with bandwidth parameter, σ_b, and centre frequency, f_c,

$$\psi(t) = \frac{1}{\sqrt{2\pi}\sigma_b} \mathrm{e}^{\mathrm{i}2\pi f_c t} \mathrm{e}^{-t^2/2\sigma_b^2}, \tag{4.2a}$$

$$W(\lambda, t) = \int_{-\infty}^{\infty} p^a(\tau) \frac{1}{\sqrt{\lambda}} \psi^* \left(\frac{\tau - t}{\lambda} \right) \mathrm{d}\tau. \tag{4.2b}$$

Note that the Morlet wavelet generalizes the Gaussian analogue (3.3) for non-vanishing frequencies $f_c \neq 0$. The corresponding Morlet filter of the antisymmetric pressure signal is denoted by $\langle p^a(t) \rangle_H$, where the subscript 'H' shall refer to the harmonic contribution. This filter is defined in terms of the inferred amplitude A_p and phase ϕ_p via

$$\langle p^a(t) \rangle_H = A_p(t) \cos(\phi_p(t)), \tag{4.3a}$$

$$\phi_p(t) = \tan^{-1}[\mathrm{Im}(W)/\mathrm{Re}(W)], \tag{4.3b}$$

$$A_p(t) = 2\sqrt{\lambda}|W(\lambda, t)|, \tag{4.3c}$$

where $\mathrm{Im}(W)$ and $\mathrm{Re}(W)$ are the imaginary and real parts of W. The centre frequency was set equal to the shedding frequency, $f_c = f_s$. Note that λf_c is the frequency filtered with the Morlet template. Setting the Morlet wavelet scale parameter to $\lambda = 1$ effectively filters the first harmonic f_s. The bandwidth parameter is set to $\sigma_b = \sqrt{3/4}/f_c$, which corresponds to five oscillation times for the filter. Note that the results were found to be insensitive to the bandwidth chosen. The Morlet wavelet is shown in figure 7. An analysed portion of a signal is shown in figure 8.

The analysing wavelet is assumed to have a constant centre frequency. Variations of the shedding frequency and amplitude are implicitly given by $\phi_p(t)$ and $A_p(t)$ obtained from the wavelet transform due to the spectral bandwidth of the Morlet wavelet employed.

The short-time-averaged symmetric pressure is determined with a Gaussian kernel according to

$$\langle p^s(t) \rangle_G = \int_{-\infty}^{\infty} p^s(\tau) g(\tau - t)\, \mathrm{d}\tau. \tag{4.4}$$

https://doi.org/10.1017/jfm.2013.494 Published online by Cambridge University Press

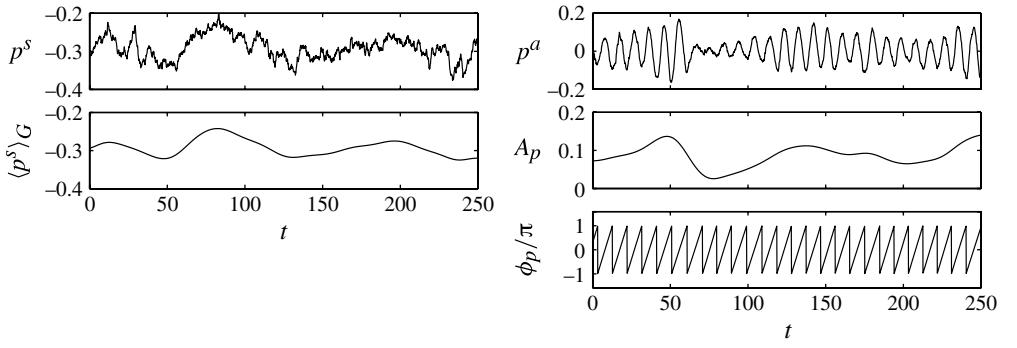


FIGURE 8. Surface pressure filtering, determining $A_p(t)$, $\phi_p(t)$, and $\langle p^s(t) \rangle_G$.

The Gaussian kernel, $g(t)$, was already used for the base flow extraction (3.3) and has the same bandwidth, σ_b, as for the wavelet transform (4.2).

4.3. *Pressure–velocity correlation*

We assume a linearly related pressure and velocity field. The local state of the flow in each PIV plane is characterized by A_1, ϕ_1, and a_Δ. Similarly, the pressure is described by A_p, ϕ_p and the mean. The amplitude of the symmetric shift mode is linked to the short-time-averaged symmetric pressure signal $\langle p^s \rangle_G$ via an affine relationship. The amplitude A_1 and phase ϕ_1 of the antisymmetric first harmonics $\widetilde{\boldsymbol{u}}_1$ are linearly correlated to the corresponding quantities of the antisymmetric pressure signal. In addition, the amplitude of the second harmonics is affinely related to the amplitude of the first harmonics. Summarizing,

$$a_\Delta = d_0 + d_1 \langle p^s \rangle_G, \tag{4.5a}$$

$$\cos\phi_1 = b_1 \cos\phi_p + b_2 \sin\phi_p, \tag{4.5b}$$

$$\sin\phi_1 = b_3 \cos\phi_p + b_4 \sin\phi_p, \tag{4.5c}$$

$$A_1 = c_0 + c_1 A_p, \tag{4.5d}$$

$$\phi_2 = 2\phi_1 + \tau, \tag{4.5e}$$

$$A_2 = k A_1^2. \tag{4.5f}$$

All coefficients $d_0, d_1, b_1, \ldots, k$ are determined by linear regression. A small time lag was introduced in the shift mode amplitude a_Δ for the best correlation (least residual) between $\langle p^s \rangle_G$ and a_Δ (Schlegel *et al.* 2012).

4.4. *Traditional phase-average implementation*

For the purpose of comparison, the implemented traditional phase-averaging procedure is briefly described. Following the triple decomposition of Reynolds & Hussain (1972) in (3.1*a*), the base flow is taken as the mean flow $\boldsymbol{u}_B(\boldsymbol{x})$. The coherent contribution, $\boldsymbol{u}_\phi(\boldsymbol{x}, \phi)$, is the ensemble average fluctuation away from the mean for the shedding phase ϕ. The instantaneous phase is determined from the antisymmetric part of the common pressure reference signal p^a using a Morlet wavelet filter as described above. The amplitude is frozen to the average value. The procedure is repeated for each uncorrelated PIV plane. The three-dimensional reconstruction is obtained by combining the results. Note that, by definition and unlike the generalized phase

https://doi.org/10.1017/jfm.2013.494 Published online by Cambridge University Press

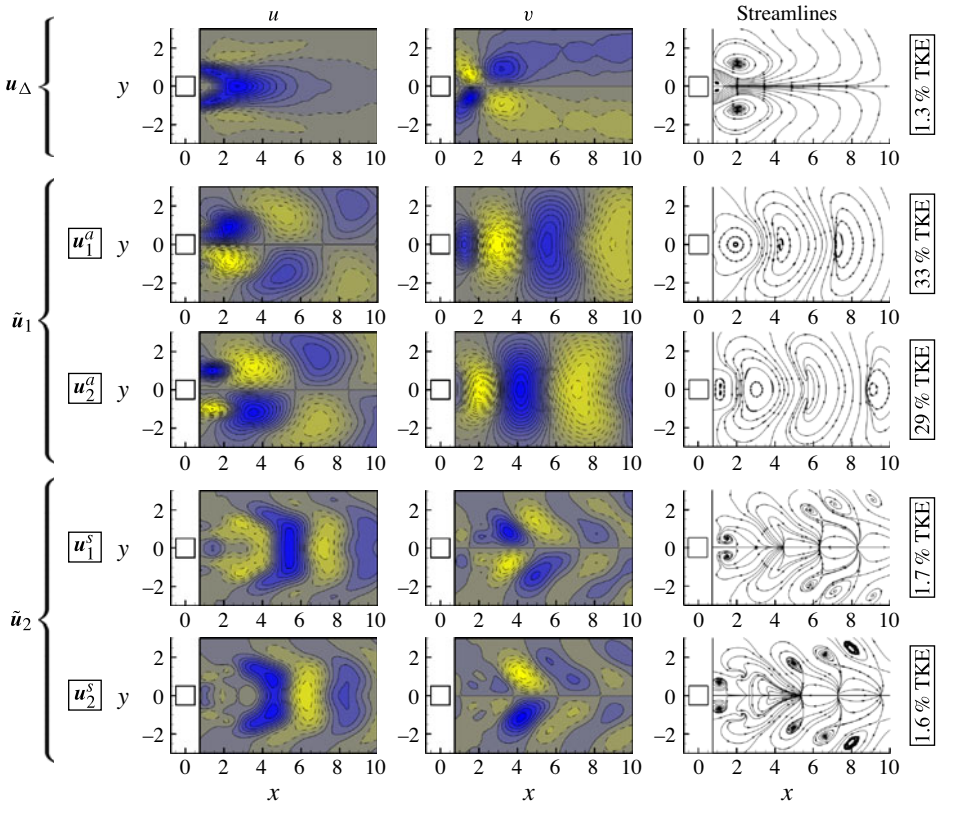


FIGURE 9. (Colour online) Two-dimensional POD modes in the plane $z = 1.25$. Shown are the contours and streamlines of the in-plane velocity components. The dashed lines indicate negative contours. Columns correspond to velocity components and modes correspond to rows. TKE comprises only the two in-plane velocity components.

average, local variations of phase cannot be accommodated using the traditional approach. Additional details for this procedure can be found in Bourgeois *et al.* (2011).

5. Results for PIV data

In this section, the generalized phase average is applied to the wall-mounted finite ($h/d = 4$) square cylinder wake. The generalized phase-average analysis of the individual PIV planes is discussed. First (§ 5.1), the modes for zeroth to second harmonic are presented. In § 5.2, the residual of the traditional and generalized phase-averaged velocity fields are investigated and reveal the advantages of incorporating low-frequency modulations.

5.1. *Modes*

Examples of the two-dimensional modes are shown for the plane $z = 1.25$ and $y = 0.25$, as determined according to the generalized phase average, in figures 9 and 10. In both planes, the two most energetic modes correspond to the fundamental frequency. The shift mode, representing the base flow variations, and the second harmonic modes contribute roughly similarly to the TKE content.

https://doi.org/10.1017/jfm.2013.494 Published online by Cambridge University Press

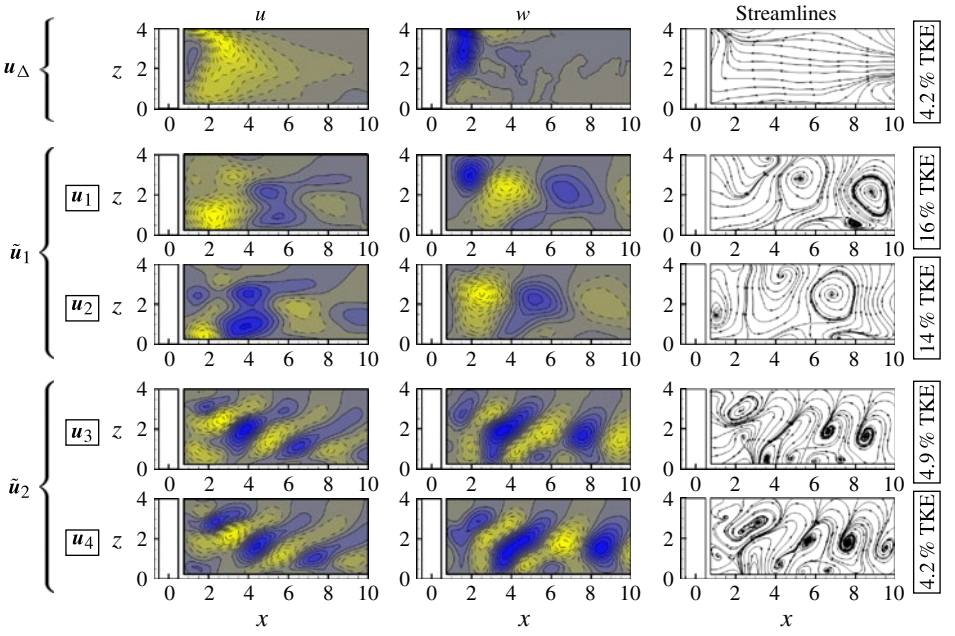


FIGURE 10. (Colour online) As in figure 9, but for the plane $y = 0.25$.

5.2. *Residuals*

The generalized phase-average results, as compared with the traditional analogue, leads to a reduction of the residuals of the filtered two-component velocity fields, $\hat{\boldsymbol{u}}$, over each PIV plane. The residuals, normalized by the mean square fluctuation, are given by

$$Z := \frac{\displaystyle\int_\Omega (\boldsymbol{u} - \hat{\boldsymbol{u}}) \cdot (\boldsymbol{u} - \hat{\boldsymbol{u}})\, \mathrm{d}A}{\displaystyle\int_\Omega \boldsymbol{u}'' \cdot \boldsymbol{u}''\, \mathrm{d}A} = \frac{\|\boldsymbol{u} - \hat{\boldsymbol{u}}\|_\Omega^2}{\overline{\|\boldsymbol{u}''\|_\Omega^2}} \tag{5.1}$$

where $\boldsymbol{u}$ is the PIV data, $\hat{\boldsymbol{u}}$ is the estimate according to the (generalized) phase average, and $\boldsymbol{u}'' := \boldsymbol{u} - \boldsymbol{U}$. These residuals can be physically interpreted as the average ratio of the expansion residual to the total measured fluctuation kinetic energy.

In figure 11, the generalized phase average shows relatively constant residual levels, evidence that amplitude modulations due to the coherent base flow variations are captured (i.e. separated from the stochastic component). In contrast, for the traditional phase average, the instantaneous residuals often exceed 20 % (corresponding to normalized residuals of over 60 %, which implies that the stochastic contribution exceeds that of the resolved kinetic energy). The mean residuals are 15 % lower for the generalized ($\approx$0.32) compared with the traditional ($\approx$0.37) phase average, indicating an important portion of the coherent fluctuations have been resolved additionally. The instantaneous differences can thus be dynamically very significant, particularly when the fluctuation amplitude, A, increasingly deviates from that of the limit cycle, $\bar{A}$.

Ensemble averages of the residuals are obtained for different values of A and a_Δ, respectively, in figures 12 and 13. As would be expected close to the limit cycle, the residuals for the two methods are very similar. However, as one deviates from the limit

https://doi.org/10.1017/jfm.2013.494 Published online by Cambridge University Press

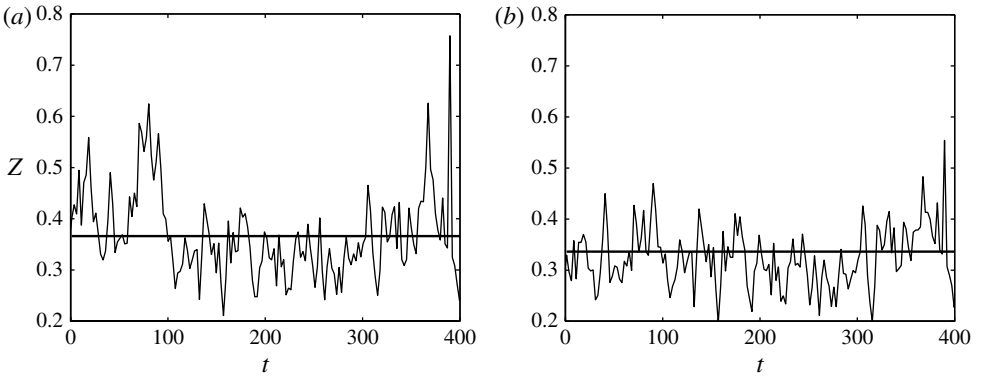


FIGURE 11. Excerpt of time traces and mean values of normalized residuals, Z, for the traditional phase average (a) and the generalized phase average (b) in the plane $z = 1.25$.

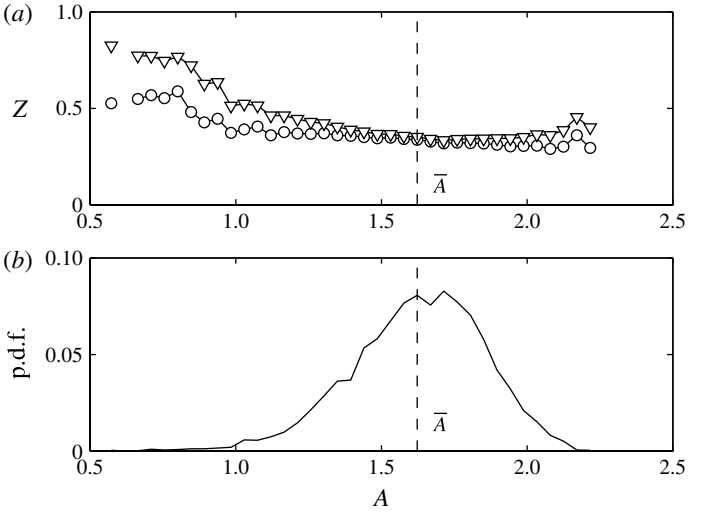


FIGURE 12. Normalized residual Z in the plane $z = 1.25$. In the top figure Z is conditionally averaged based on the amplitude A for the traditional ($\triangledown$) and generalized phase average ($\bigcirc$) The bottom figure displays the p.d.f. of A.

cycle, the residuals grow very fast for the traditional phase average. These can be in excess of 30 % greater than the residuals for the generalized phase average. The latter shows fairly flat residuals over variations of A or a_Δ. The probability density functions (p.d.f.) for A and a_Δ show that even for large excursions from $\overline{A}$ or $a_\Delta = 0$, the generalized phase average retains a good characterization of the flow. Thus, there is a clear advantage to using generalized phase-average data for calibration when trying to construct dynamical models of the flow.

6. Results for three-dimensional flow estimation

The correlation between surface pressures and mode amplitudes allows a temporal interpolation of the data (§ 6.1). In § 6.2 mode amplitudes computed from PIV and

https://doi.org/10.1017/jfm.2013.494 Published online by Cambridge University Press

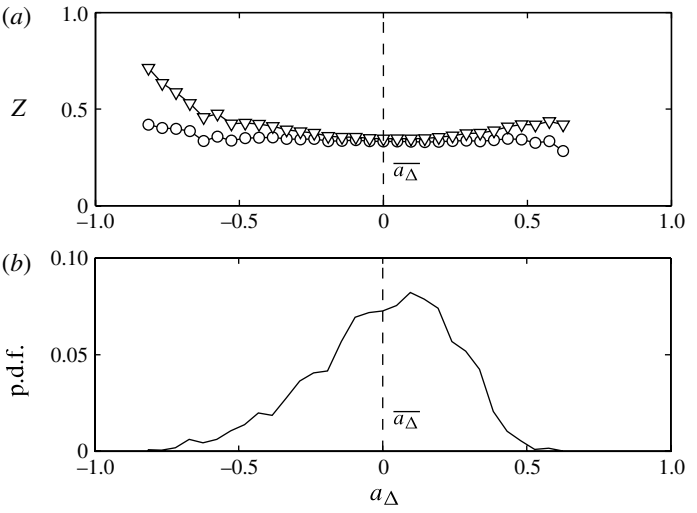


FIGURE 13. Same as figure 12, but for the shift mode amplitude a_Δ instead of the oscillation amplitude A.

estimated from the pressure sensors are compared. Finally (§ 6.3), the estimated three-dimensional flow with corresponding modes are presented and the resulting least-order model is elaborated on in appendix B.

6.1. *Pressure–velocity correlation*

The correlation of the POD modes with the surface pressure is required to link the independently acquired PIV planes and construct the global flow estimation in § 6.3. In § 6.2, we compare the flow state, represented by $a_i(t)$, obtained by the original generalized phase average and compare it with the state estimated using the simultaneous pressure measurements.

Figure 14 shows the parameters of the generalized phase average (grey symbols) for $z = 1.25$ in the wake along with their estimation curves (black) deduced from the velocity POD–pressure data correlations. The shedding phase obtained from the generalized phase average, ϕ, and that from the filtered antisymmetric pressure, ϕ_p, as in figure 14(*a*) differ little. Comparing the amplitude of oscillation, A, in figure 14(*b*), the amplitude of the pressure is positively correlated with the amplitude of the first harmonic mode. The zero of the harmonic amplitude of the linear fit is far from zero of the pressure amplitude and indicates mode deformations (Tadmor *et al.* 2010). The propensity for oblique-type shedding and other three-dimensional changes to the vortex-shedding structure are expected in this flow (Bourgeois *et al.* 2011) and the modelling implications are addressed later. The Gaussian filtered symmetric pressure and the shift mode again shows good linearity between the two signals (see figure 14*c*).

6.2. *Dynamics of mode amplitudes*

Figure 15 shows the observed values of the first and second antisymmetric modes (grey points). Superimposed is the (traditional) phase-averaged amplitude (solid line). It is clear that while the phase-averaged amplitude is a typical representation of the field, the dynamically important amplitude modulation cannot be represented.

https://doi.org/10.1017/jfm.2013.494 Published online by Cambridge University Press

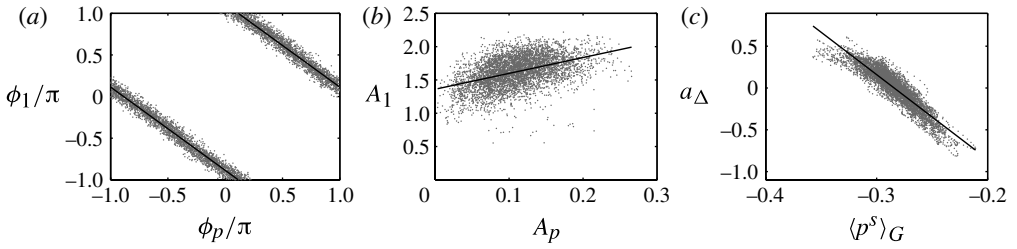


FIGURE 14. Pressure–velocity correlation for $z = 1.25$: (*a*) harmonic phase; (*b*) harmonic amplitudes; (*c*) shift mode amplitude versus mean pressure.

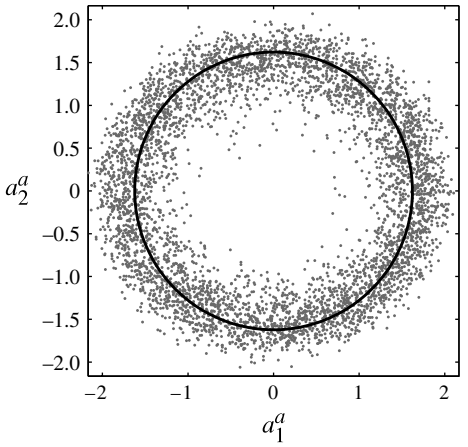


FIGURE 15. Phase portrait of the POD mode amplitudes, a_1^a, a_2^a, representing the first harmonic for the plane $z = 1.25$. The solid line shows the traditional phase-averaged amplitude.

The benefit of the generalized phase average is that this amplitude modulation can be approximated by modelling the interdependence of the more energetic mode amplitudes (in this case shift, first and second harmonic modes) linked by the snapshot pressure fluctuation.

Figures 16–18 show the shift mode, the first and the second harmonics. On the left-hand side, the predicted amplitudes from the pressure signal (solid line) are compared with the POD values from the original velocity field snapshots (symbols). On the right-hand side of these figures, the scatter plot of the observed amplitudes against the phase is shown along with the curves corresponding to the phase average. Figure 16 shows that the slowly varying shift mode amplitude is well predicted from the (Gaussian-filtered) symmetric pressure. Note that, by definition, the shift mode is identically zero for the phase-averaged representation. In figure 17(*a*), the amplitude modulation of the first harmonics are well predicted using the antisymmetric pressure. The right-hand figure shows that excursions from the phase-average amplitude can now be represented, making the generalized phase average a better description off of the limit cycle.

Figure 18 shows the second harmonic components. The estimation obtained from the pressure is indirect using a slaving $A_2 = kA_1^2$ and $\phi_2 = 2\phi_1 + \tau$ following Dušek

https://doi.org/10.1017/jfm.2013.494 Published online by Cambridge University Press

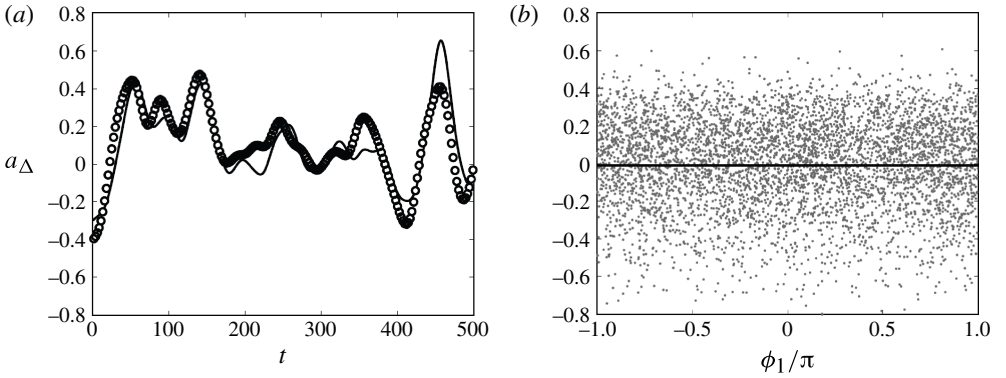


FIGURE 16. (*a*) Observed (symbols) shift mode amplitudes and estimations (solid line) from the pressure for the plane $z = 1.25$. (*b*) Shift mode amplitudes over the phase, ϕ_1. The traditional phase average for the shift mode is by definition identically zero (solid line).

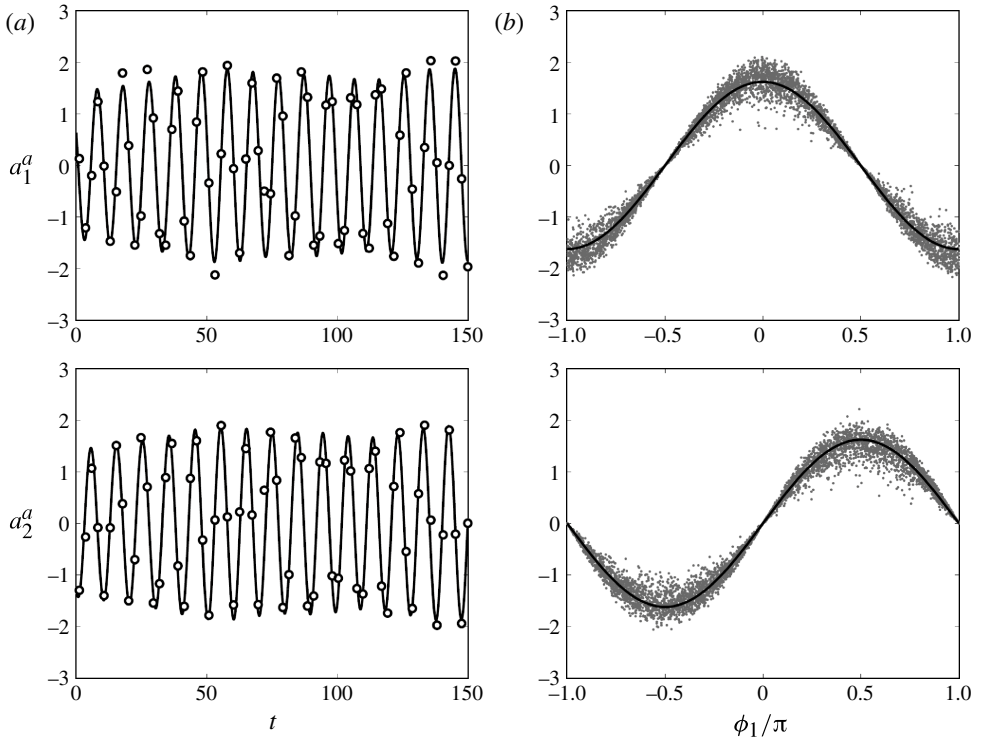


FIGURE 17. (*a*) Observed (symbols) first harmonic POD mode amplitudes and estimations (solid line) from the pressure for the plane $z = 1.25$. (*b*) First harmonic POD mode amplitudes over the phase, ϕ_1. Also shown is the curve of the phase-averaged amplitude.

et al. (1994) for laminar wakes. While additional sensors could help make the estimation of the second harmonic more accurate, the present agreement is still quite good and the eigenmodes obtained display a good characterization of the mode shapes.

https://doi.org/10.1017/jfm.2013.494 Published online by Cambridge University Press

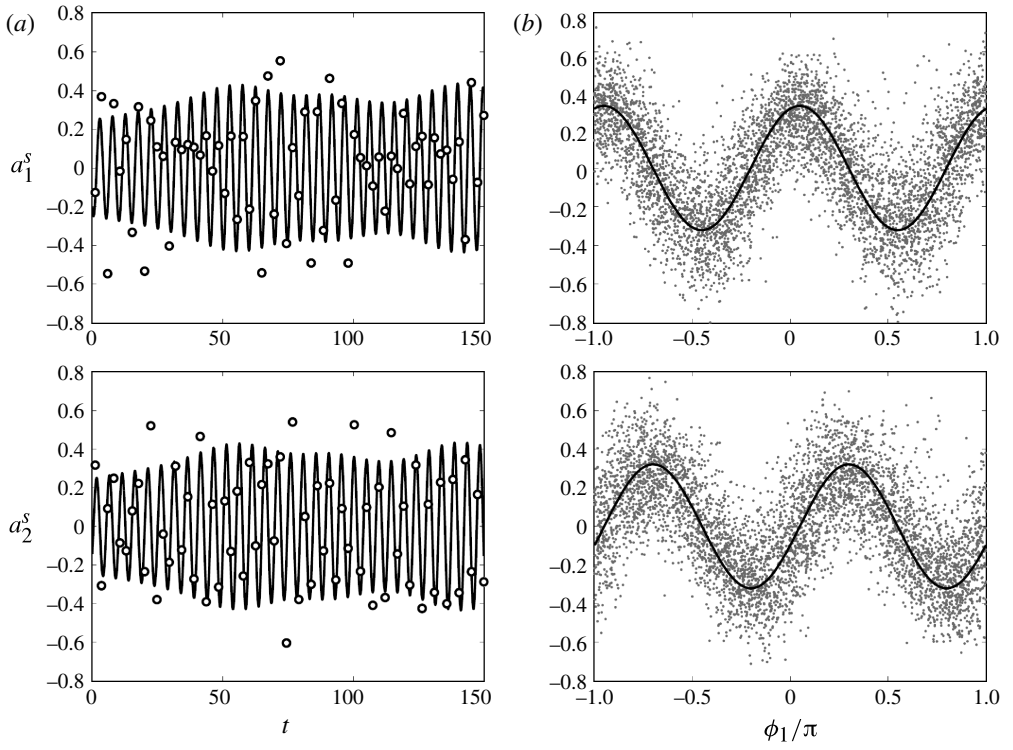


FIGURE 18. As for figure 17, but for the second harmonic POD modes.

These modes can therefore be implemented in the global flow estimation. Again, very significant excursions are found throughout the data from the phase-averaged amplitude, making the latter a poor dynamic representation.

6.3. *Three-dimensional flow estimation*

After the parametrization of all the PIV planes, a set of three-component velocity field snapshots in three-dimensions can be estimated from a given measured pressure signal. The generalized phase average is carried out on the snapshots of this global velocity field to obtain global POD modes. Isosurfaces of these modes are shown in figures 19–21.

The snapshot mode amplitudes are plotted against the pressure phase and amplitude in figures 19–21 (right-hand side). The first harmonic is clearly dominant. Each mode in the pair correspond to 46.5 % of the resolved TKE. Each mode of the second harmonic accounts for only ∼2.2 % of the TKE, but plays an important role in describing the fluctuations in the centre of the wake. These fluctuations will be related to the vortical strands connecting subsequently shed vortices observed earlier (Bourgeois *et al.* 2011). The shift mode, active away from the limit cycle, has a similar energy to the second harmonic with 2.3 %.

In figure 22, the three-dimensional construction of the flow field based on the global modes according to

$$\boldsymbol{u} = \boldsymbol{U} + a_{\Delta}\boldsymbol{u}_{\Delta} + \sum_{i=1}^{2} a_i^a \boldsymbol{u}_i^a + \sum_{i=1}^{2} a_i^s \boldsymbol{u}_i^s \tag{6.1}$$

https://doi.org/10.1017/jfm.2013.494 Published online by Cambridge University Press

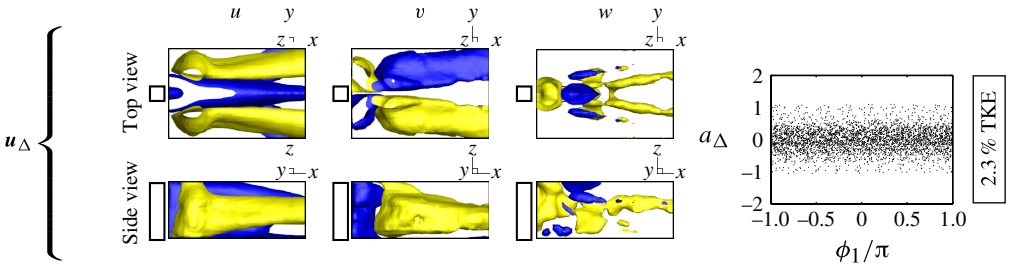


FIGURE 19. (Colour online) Three-dimensional reconstructed shift mode (isosurfaces of ± 0.02). Percentage of TKE stated is for the three-dimensional estimated flow.

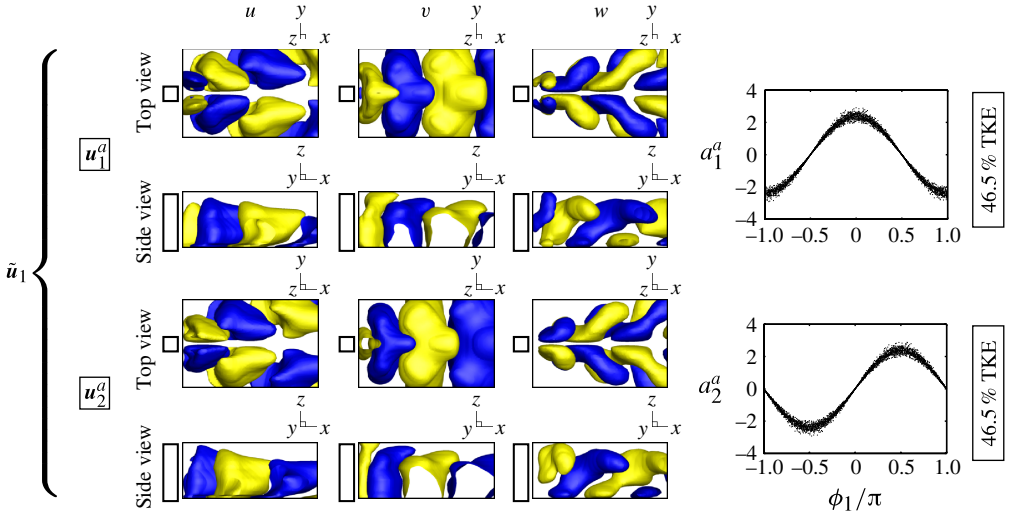


FIGURE 20. (Colour online) Same as figure 19, but for the first harmonic modes.

is shown for the values of a_i on the limit cycle ($a_\Delta = 0$, $a_1^a = \overline{A}_1 \cos\phi_1$, $a_2^a = \overline{A}_1 \sin\phi_1$, $a_1^s = \overline{A}_2 \cos(2\phi_1 + \tau)$ and $a_2^s = \overline{A}_2 \sin(2\phi_1 + \tau)$). The coherent vortical structures are identified by the Okubo–Weiss parameter $Q = (\|\boldsymbol{\Omega}\|^2 - \|\boldsymbol{S}\|^2)/2$, where Ω and $\boldsymbol{S}$ are the antisymmetric and symmetric part of the velocity Jacobian $\boldsymbol{\nabla u}$, respectively, and $\|\,\|$ denotes the standard Euclidean norm (Hunt, Wray & Moin 1988). For incompressible flows, $2Q$ is the source term of the pressure Poisson equation $\Delta p = 2Q$. Evidently, the isosurface $Q = 0.04$ describe half-loops. The initially vertical vortices shed along the side faces of the cylinder deform towards the free-end creating connector strands, which tie together subsequently shed principal cores of the structures (Bourgeois *et al.* 2011). Contours of the u and w fields in the planes $z = 2$ and $y = 0$ show the typical signatures of the large-scale vortices in the field. Oscillations of the u and w components within the plane of symmetry $y = 0$ are due only to the even harmonics because for antisymmetric modes $u^a(y = 0) = w^a(y = 0) = 0$. The oscillations in the field due to the connector strands are therefore dominated by the second harmonic in this plane.

https://doi.org/10.1017/jfm.2013.494 Published online by Cambridge University Press

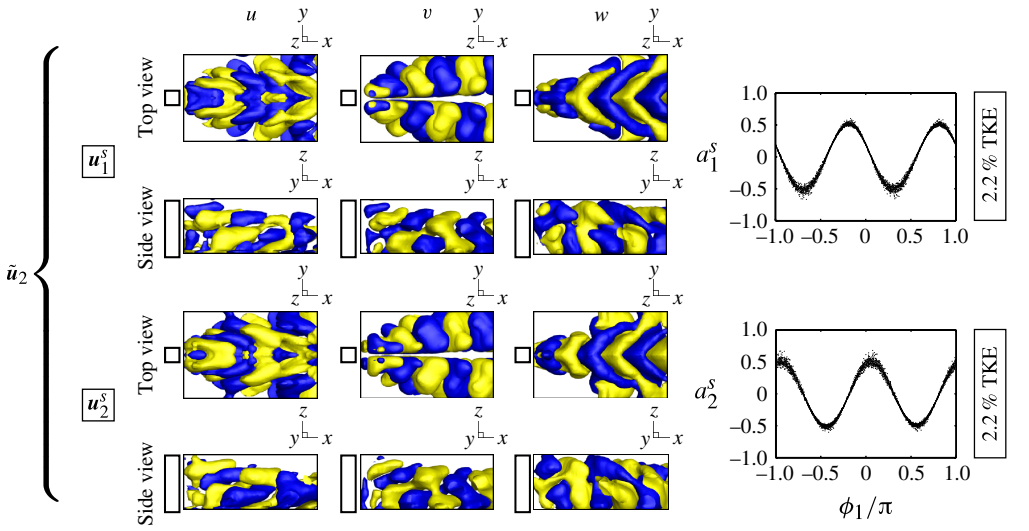


FIGURE 21. (Colour online) Same as figure 20, but for the second harmonic modes.

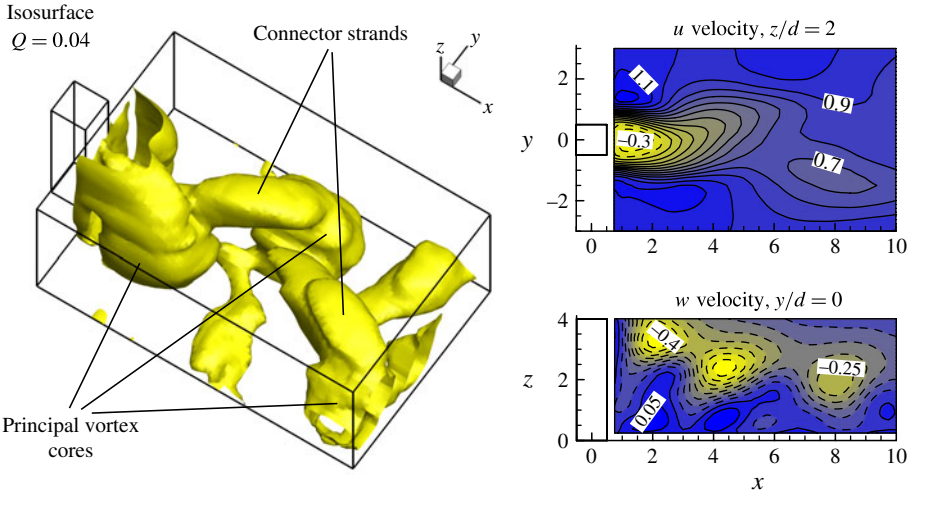


FIGURE 22. (Colour online) Vortex structures identified with $Q = 0.04$ and contours of the velocity field predicted by the reduced-order representation on the limit cycle $a_\Delta = 0$.

The additional dynamics that can be captured with the generalized phase average are the modulation of the amplitude of oscillation and the reaction of the base flow field. Figure 23 shows the changes to the base flow field for different shift mode levels $a_\Delta \in \{-1, 0, 1\}$. The most prominent feature is a change in the size of the recirculation zone, which can be characterized by the recirculation length l_r determined from the position along the $y = 0$ in the plane $z = 1$. The shift mode is also coupled to the amplitude of the first harmonic oscillation, which can be estimated from the algebraic relationship $a_\Delta = B_{FP} + c_1 A_1^2$ (see appendix A). On the limit cycle, $a_\Delta = 0$, the amplitude of oscillation is $A_1 = 2.4$ and $l_r = 2.6$. Presumably A_1 is a measure

https://doi.org/10.1017/jfm.2013.494 Published online by Cambridge University Press

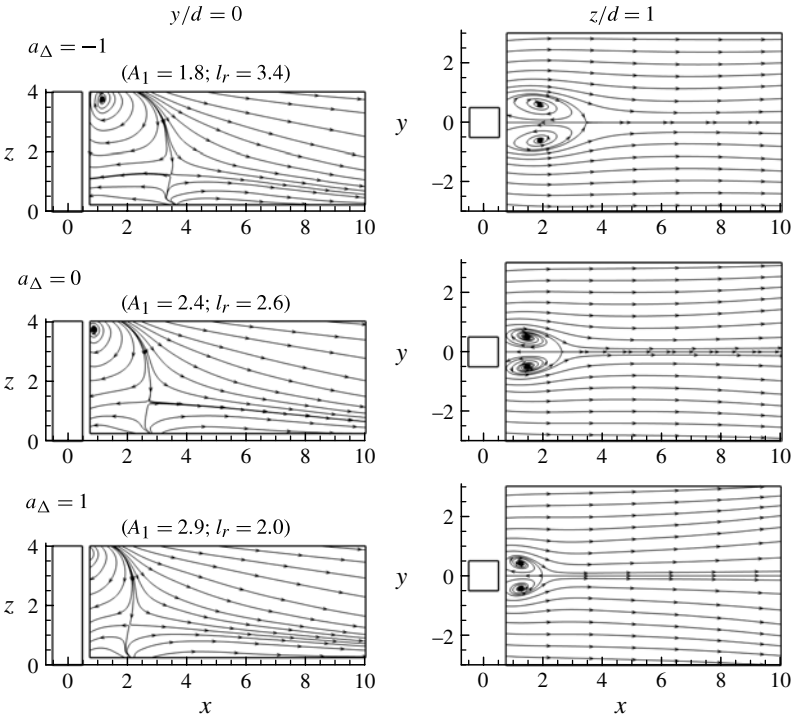


FIGURE 23. Modified base flow, $\boldsymbol{u}_B = \boldsymbol{U} + a_\Delta \boldsymbol{u}_\Delta$, for different values of the shift mode, a_Δ.

of the strength (circulation) of the shed vortices. Furthermore, the length of the lee recirculation region should vary inversely with the strength of the shed vortex. This expectation is satisfied in the observed model behaviour. When the oscillatory amplitude is $A_1 = 1.8$, a value below the attractor amplitude, $a_\Delta = -1$ and the recirculation length is longer, $l_r = 3.4$. For an amplitude of $A_1 = 2.9$, $a_\Delta = 1$ and the recirculation length is reduced to $l_r = 2.0$.

Capturing the coherent cycle-to-cycle variations is of practical significance, both from fundamental and applied perspectives. These variations are not captured with traditional phase-averaging techniques as illustrated by Sattari *et al.* (2012). For example, figure 24 shows the distribution of the coherent vertical velocity component w in the obstacle wake along the plane $x/d = 2$ for an arbitrary shedding phase. The top row in this figure shows the base flow, while the bottom row depicts the generalized phase average. Considering the base flow during low-amplitude cycles ($a_\Delta = -1$), the maximum w-magnitude occurs roughly at the elevation of the obstacle free-end. In contrast, during high-amplitude cycles ($a_\Delta = 1$), the maximum magnitude of w occurs much deeper in the obstacle wake and is more than 2.5 times larger. From the generalized phase average, it is seen that this downward motion is amplified by the passage of the vortices, such that the downward motion is stronger and penetrates deeper into the wake during high-amplitude than during low-amplitude cycles. This effectively constitutes a velocity downburst. As can be inferred from figure 25, regions of strong downflow are intimately related to the location of the tilted vortex strands. Thus, the slow-drift contribution to the base flow impacts the wake downwash both directly and indirectly by causing a reorganization of the vortex structures. Fundamentally, these large variations in w imply differences

https://doi.org/10.1017/jfm.2013.494 Published online by Cambridge University Press

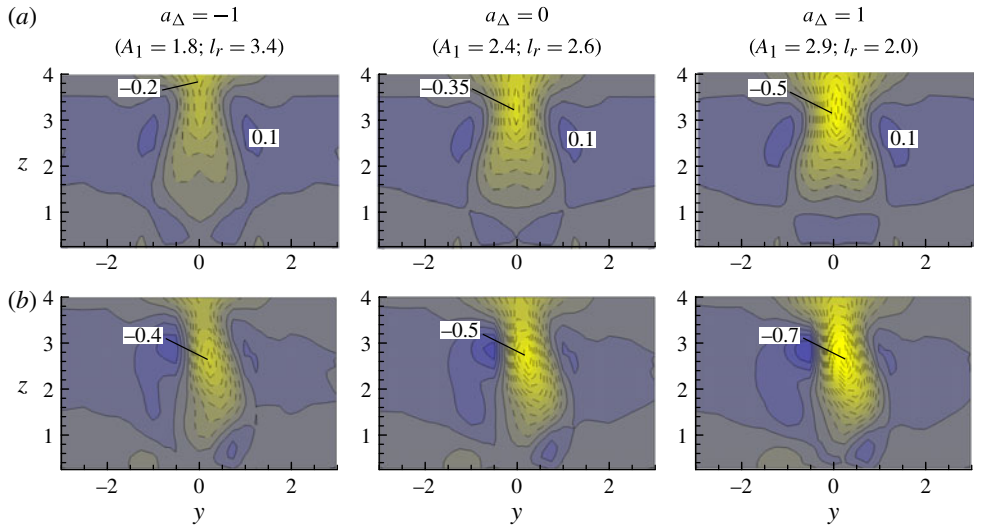


FIGURE 24. (Colour online) Isocontours of the resolved vertical flow component w for different values of the shift mode, a_Δ, in the plane $x = 2$. Top row (a) represents the base flow. Bottom row (b) shows the generalized phase average.

in cycle-to-cycle energy distribution amongst fluctuation scales. These variations are inappropriately associated with stochastic fluctuations using traditional phase averaging with the implied constant base flow and constant fluctuation level. These strong downward velocity events impact scalar transport and ground-level gusts. Their reliable characterization is thus an important consideration, for example, in wind engineering for pedestrian-level safety and comfort.

Figure 26 displays the observed behaviour of a_Δ and A_1^2. The shift mode and amplitude values have been estimated independently from the correlations with the pressure sensors. The data show a remarkable linearity between a_Δ and A_1^2, corroborating the assumptions in the mean field model discussed in appendix A.

The mean field model is a reduced-order Galerkin system determined for the first two harmonic mode pairs, a_1^a, a_2^a (first harmonic) and a_1^s, a_2^s (second harmonic), and the shift mode, a_Δ. The main behavioural characteristics of the observed system can be deduced from figure 27. The mean-field paraboloid relating the shift mode and first harmonic amplitude is clearly rendered. Typical Lissajou phase portraits emphasize that the phase dynamics are slaves of the mean-field paraboloid.

The model retains the shift mode and first harmonic coupling as well as the driving of the second harmonic by the first. In order to account for the stochastic amplitude modulation observed, a noise term is inserted into the model whereby the state of the system is continuously perturbed off the periodic solution as the model draws the system back to the periodic state. The nearly periodic solution of the experimental mode amplitudes is reasonably well approximated as detailed in appendix A.

7. Conclusions

We present a generalized phase-averaging technique accounting for low-frequency modulation of the base flow, of the oscillation amplitude and frequency, and of higher harmonics. This methodology enables the sensor-based time-resolved construction of a

https://doi.org/10.1017/jfm.2013.494 Published online by Cambridge University Press

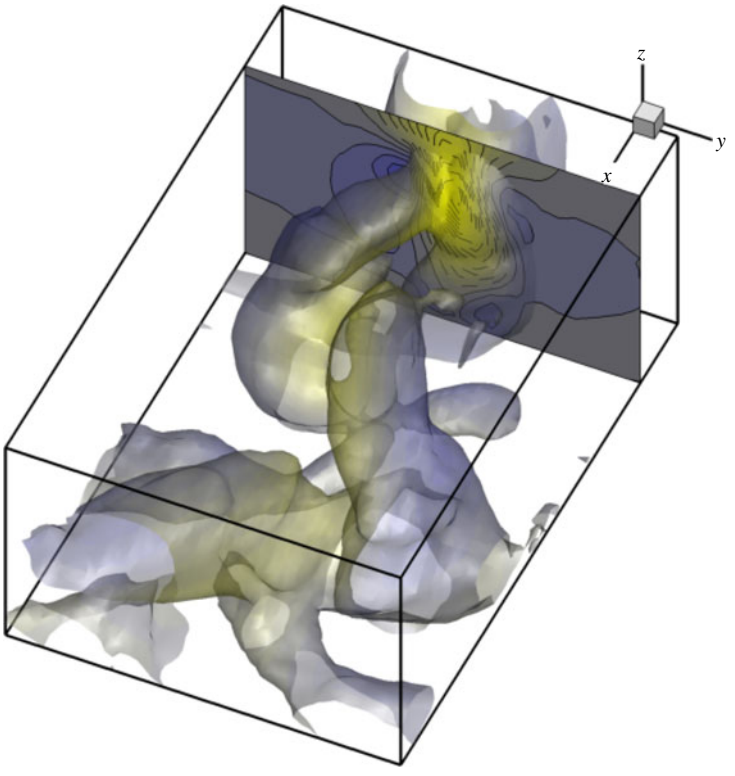


FIGURE 25. (Colour online) Reduced-order representation of the vortex structures for $a_\Delta = 0$ identified with $Q = 0.04$.

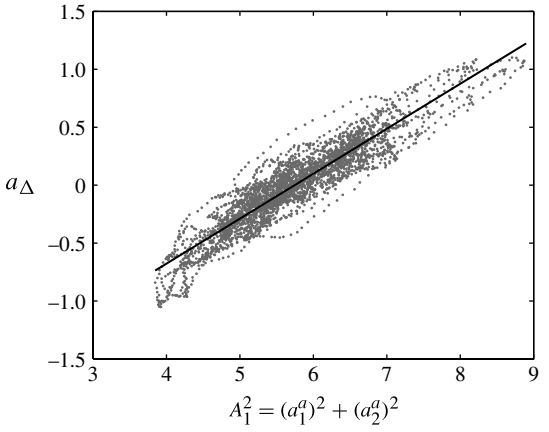


FIGURE 26. Observed (grey points) and algebraically modelled (solid line) shift mode behaviour in terms of the amplitude of the first harmonic mode pair.

three-dimensional flow field from independently acquired orthogonal two-dimensional PIV planes. The PIV snapshots have been synchronized with reference pressure sensors. This approach was applied to the turbulent nearly periodic wake flow of a

https://doi.org/10.1017/jfm.2013.494 Published online by Cambridge University Press

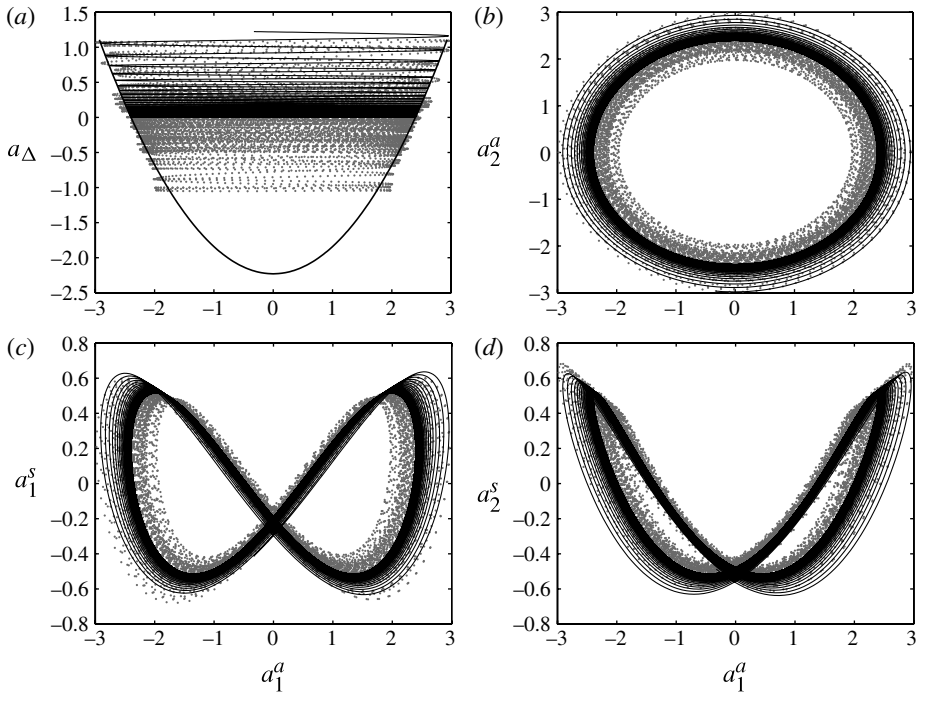


FIGURE 27. Observed generalized phase-average (grey points) and traditional phase-average (solid line) mode behaviour. The mean field paraboloid is also sketched in the top left figure for reference.

vertical surface-mounted square-section cylinder of aspect ratio 4. A reduced-order representation was formulated using modes for zeroth, first and second harmonics. The resulting estimation of the coherent wake flow field elucidated the spatiotemporal evolution of the three-dimensional large-scale wake structures.

The proposed methodology goes beyond traditional phase-averaging techniques which identify the flow state with a single phase. The resulting limit cycle has constant base flow and constant oscillation amplitude. The proposed generalized phase average also describes the flow field away from the limit cycle. It has several discriminating features: first, the inclusion of the shift mode allows for resolving base flow variations; second, variable oscillation levels are accounted for; third, the second harmonic (or arbitrary higher harmonics) can also be included.

The proposed three-dimensional construction differs from linear stochastic estimation (Adrian & Moin 1988; Glauser *et al.* 1999; Taylor & Glauser 2004) extended POD (Borée 2003) and OID (Schlegel *et al.* 2012) in several respects. First, the pressure signals are decomposed in symmetric and antisymmetric signals, thus each (anti)symmetrized signal connects directly to the base flow and to the first harmonic. Second, the (anti)symmetrized signals are Gaussian filtered for estimating base flow variations. Third, the signals are Morlet filtered to distill amplitude and phase of the first harmonics, which is related to same quantities of the generalized phase average of the flow field. Thus, high-frequency noise is filtered out. Fourth, the second harmonic is estimated from the first harmonics via an empirically fitted relation. Summarizing, the link between the zeroth, first and second harmonics of the pressure signal and the three-dimensional velocity field is established on

https://doi.org/10.1017/jfm.2013.494 Published online by Cambridge University Press

corresponding spatiotemporal subspaces. The construction using the generalized phase average implicitly accounts for non-periodic deviations in addition to a globally defined shedding phase for flow field estimation.

The generalized phase average flow parametrization is underpinned by a least-order dynamical model linking base flow oscillations and stochastic flow components. A surprisingly good agreement between model and experiment is achieved by a simple generalized mean field consideration and multiplicative noise term (see appendix A). The framework developed herein can be generalized to cases where multiple base frequencies exist (cf. Luchtenburg *et al.* 2009). This further generalization allows for accessible separation and analysis of complex flow structures.

Further benefits of such a flow decomposition have also been presented. One is the ability to use the decomposition for three-dimensional flow estimation using few select sensors such as the surface pressure. Also the generalized phase average can be used for an increased resolution of coherent structure dynamics. Such aspects include changes of the growth rates and mean-field relations resolving stabilizing mechanisms of the non-periodic attractor.

Acknowledgements

The authors acknowledge the funding and excellent working conditions of the Chaire d'Excellence 'Closed-loop control of turbulent shear flows using reduced-order models' (TUCOROM) of the French Agence Nationale de la Recherche (ANR). We are grateful to the Ambrosys Ltd. Society for Complex Systems Management and the Bernd Noack Cybernetics Foundation for additional support. We appreciate valuable stimulating discussions with M. Abel, S. Krajnović, R. Niven, M. Schlegel, G. Tadmor, B. Protas and J.-E. Wesfreid as well as the local TUCOROM team: J. Borée, J.-P. Bonnet, L. Cordier, J. Delville, P. Jordan, V. Parezanović and A. Spohn. We also thank the anonymous reviewers for their insightful suggestions and comments.

Appendix A. Towards a dynamical system of the three-dimensional flow

In this appendix, a least-order model is developed for the temporal evolution of the constructed three-dimensional velocity field. This model shall comprise the resolved part of the triple decomposition

$$\boldsymbol{u} = \underbrace{\boldsymbol{u}_0 + a_\Delta \boldsymbol{u}_\Delta}_{\boldsymbol{u}_B} + \underbrace{a_1^a \boldsymbol{u}_1^a + a_2^a \boldsymbol{u}_2^a + a_1^s \boldsymbol{u}_1^s + a_2^s \boldsymbol{u}_2^s}_{\boldsymbol{u}_\phi} + \boldsymbol{u}_S, \tag{A 1}$$

i.e. includes the shift mode amplitude a_Δ and the first and second harmonics a_1^a, a_2^a, a_1^s and a_2^s. The stochastic component shall be simulated by a noise term in the model.

For simplicity, let $\boldsymbol{u}_i$, $i = 1, \ldots, 5$ be the modes of (A 1), i.e. $\boldsymbol{u}_1 = \boldsymbol{u}_1^a$, $\boldsymbol{u}_2 = \boldsymbol{u}_2^a$, $\boldsymbol{u}_3 = \boldsymbol{u}_1^a$, $\boldsymbol{u}_4 = \boldsymbol{u}_2^s$ and $\boldsymbol{u}_5 = \boldsymbol{u}_\Delta$, and let a_i be the corresponding amplitudes. In the following, we perform a structure identification of the corresponding dynamical system without noise. The modes representing the first and second harmonics are an orthonormal system by construction: $\boldsymbol{u}_1$ and $\boldsymbol{u}_2$ are POD modes of the antisymmetric subspace and hence are orthonormal. Similarly, $\boldsymbol{u}_3$ and $\boldsymbol{u}_4$ are POD modes of the symmetric subspace and hence are also orthonormal. Moreover, symmetric and antisymmetric subspaces are orthogonal to each other, concluding the proof of orthonormality. The fifth mode (shift mode) is Gram–Schmidt orthonormalized with respect to the first four modes. A Galerkin projection of the Navier–Stokes equation

https://doi.org/10.1017/jfm.2013.494 Published online by Cambridge University Press

onto the five-mode expansion yields a system of ordinary differential equations:

$$\frac{\mathrm{d}a_i}{\mathrm{d}t} = c_i + \sum_{j=1}^{5} l_{ij}a_j + \sum_{j,k=1}^{5} q_{ijk}a_j a_k, \quad i = 1, \ldots, 5. \tag{A 2}$$

For sufficiently large domains, the quadratic term is energy preserving (Noack 2011), i.e. has totally antisymmetric quadratic coefficients:

$$q_{ijk} + q_{ikj} + \cdots + q_{kji} = 0, \quad \forall i, j, k = 1, \ldots, 5. \tag{A 3}$$

The strongest limitation of (A 2) is imposed by the solution

$$a_1^a = A_1 \cos(\omega_1 t) \tag{A 4a}$$
$$a_2^a = A_1 \sin(\omega_1 t) \tag{A 4b}$$
$$a_1^s = A_2 \cos(2\omega_1 t + \tau) \tag{A 4c}$$
$$a_2^s = A_2 \sin(2\omega_1 t + \tau) \tag{A 4d}$$
$$a_\Delta = B_{FP} + B' \tag{A 4e}$$

where A_1, A_2, B' and ω_1 are slowly varying functions of time as compared with the oscillation period $T_1 = 2\pi/\omega_1$. The constant B_{FP} is chosen so that $\boldsymbol{U} + B_{FP}\boldsymbol{u}_\Delta$ represents the fixed point of the Navier–Stokes equation.

The derivation of the resulting dynamical system closely follows a generalized mean-field derivation (Noack *et al.* 2003; Luchtenburg *et al.* 2009) and leads to

$$\frac{\mathrm{d}a_1^a}{\mathrm{d}t} = (\sigma_1 - \beta_1 B' + \beta_\xi \xi)a_1^a - (\omega_1 + \gamma_1 B')a_2^a \tag{A 5a}$$
$$\frac{\mathrm{d}a_2^a}{\mathrm{d}t} = (\sigma_1 - \beta_1 B' + \beta_\xi \xi)a_2^a + (\omega_1 + \gamma_1 B')a_1^a \tag{A 5b}$$
$$\frac{\mathrm{d}a_1^s}{\mathrm{d}t} = (\sigma_2 - \beta_2 B')a_1^s - (2\omega_1 + 2\gamma_1 B')a_2^s + h_1^s \tag{A 5c}$$
$$\frac{\mathrm{d}a_2^s}{\mathrm{d}t} = (\sigma_2 - \beta_2 B')a_2^s + (2\omega_1 + 2\gamma_1 B')a_1^s + h_2^s \tag{A 5d}$$
$$\frac{\mathrm{d}B'}{\mathrm{d}t} = \sigma_\Delta B' + c_1 A_1^2 \tag{A 5e}$$
$$\frac{\mathrm{d}\xi}{\mathrm{d}t} = -\sigma_g \xi + n(t). \tag{A 5f}$$

The first oscillator (A 5*a*,*b*) describes a self-amplified amplitude-limited oscillation with growth-rate $\sigma_1 - \beta_1 B'$ damped by the base flow amplitude B' with a mean-field dependent frequency $\omega_1 + \gamma_1 B'$.

The second oscillator (A 5*c*,*d*) describes a damped oscillation with growth-rate $\sigma_2 - \beta_2 B' < 0$ and twice the frequency $2\omega_1 + 2\gamma_1 B'$. This oscillator is driven by the quadratic forcing terms

$$h_1^s = f[(a_1^a)^2 - (a_2^a)^2] + 2g a_1^a a_2^a, \tag{A 6a}$$
$$h_2^s = -g[(a_1^a)^2 - (a_2^a)^2] + 2f a_1^a a_2^a. \tag{A 6b}$$

The parameters g and f control amplitude and phase of the second harmonic. This forcing term has vanishing DC component and vanishing first harmonic terms.

https://doi.org/10.1017/jfm.2013.494 Published online by Cambridge University Press

σ_1	0.223
β_1	0.1
ω_1	0.2π
γ_1	0.03
σ_2	−0.5
β_2	0.1
f	0.0166
g	−0.0417
B_{FP}	−2.23
c_1	0.388
σ_g	0.04
β_ξ	0.12

TABLE 1. Values of coefficients of the model system (A 8).

The base flow is described by (A 5*e*) and is driven by the first harmonics. The translation (A 4*e*) implies that $a_1^a = a_2^a = a_1^s = a_2^s = B' = 0$ represents a fixed point of (A 5) at vanishing noise level $\xi \equiv 0$. Following Noack *et al.* (2003) and Luchtenburg *et al.* (2009), we exploit the slow variation of the shift mode amplitude by slaving,

$$a_\Delta = B_{FP} + c_1 A_1^2. \tag{A 7}$$

This leads to the descriptor system

$$\frac{\mathrm{d}a_1^a}{\mathrm{d}t} = (\sigma_1 - \beta_1 B' + \beta_\xi \xi) a_1^a - (\omega_1 + \gamma_1 B') a_2^a \tag{A 8a}$$

$$\frac{\mathrm{d}a_2^a}{\mathrm{d}t} = (\sigma_1 - \beta_1 B' + \beta_\xi \xi) a_2^a + (\omega_1 + \gamma_1 B') a_1^a \tag{A 8b}$$

$$\frac{\mathrm{d}a_1^s}{\mathrm{d}t} = (\sigma_2 - \beta_2 B') a_1^s - (2\omega_1 + 2\gamma_1 B') a_2^s + f[(a_1^a)^2 - (a_2^a)^2] + 2g a_1^a a_2^a \tag{A 8c}$$

$$\frac{\mathrm{d}a_2^s}{\mathrm{d}t} = (\sigma_2 - \beta_2 B') a_2^s + (2\omega_1 + 2\gamma_1 B') a_1^s - g[(a_1^a)^2 - (a_2^a)^2] + 2f a_1^a a_2^a \tag{A 8d}$$

$$B' = c_1 A_1^2 \tag{A 8e}$$

$$\frac{\mathrm{d}\xi}{\mathrm{d}t} = -\sigma_g \xi + n(t). \tag{A 8f}$$

Last but not least, the dynamics of the Langevin equation (A 8*f*) is discussed. Here $n(t)$ is a Gaussian process with vanishing mean and variance of unity. This stable noise-driven equation leads to a Wiener process $\xi(t)$. This Wiener process modulates the growth rate in (A 8*a*) and (A 8*b*) accounting for the energetic sink/source effect of the stochastic term $\boldsymbol{u}_S$. Thus, the experimentally observed amplitude variations of figure 27 are accounted for.

The calibration procedure of the coefficients in (A 8) has three steps. First, the growth rates σ_1 and σ_2 near the steady solution were estimated from physical arguments. Second, the remaining parameters were determined so that the phase-averaged limit cycle is exactly reproduced under vanishing noise. Third, the variability of the amplitudes is modelled with the noise term. Table 1 provides the calibrated parameters for (A 8).

The resulting solution of the least-order model (A 8) is depicted in figures 28–32. Figures 28 and 29 show the evolution of A_1 and a_Δ for the experiment and model

https://doi.org/10.1017/jfm.2013.494 Published online by Cambridge University Press

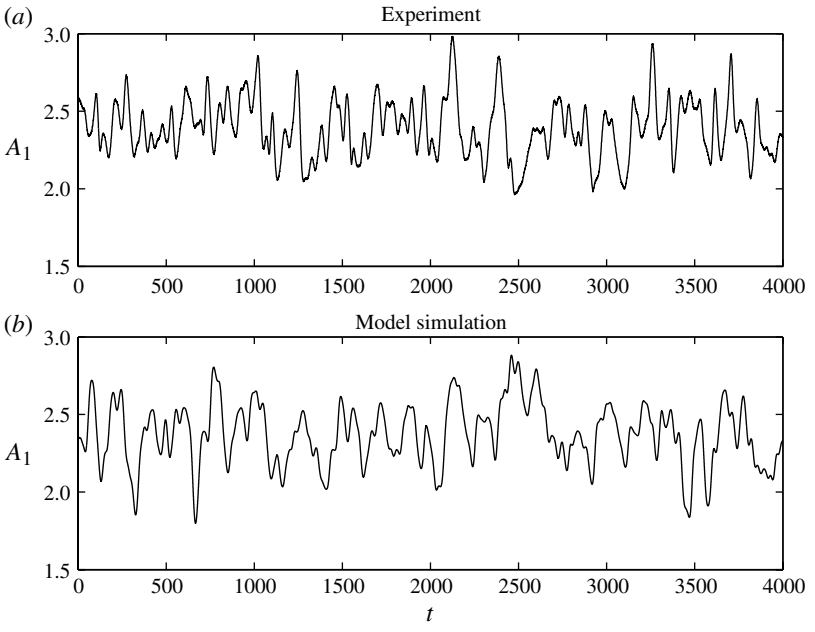


FIGURE 28. Evolution of the oscillation amplitude A_1 of (a) the experiment and (b) of the least-order model (A 8).

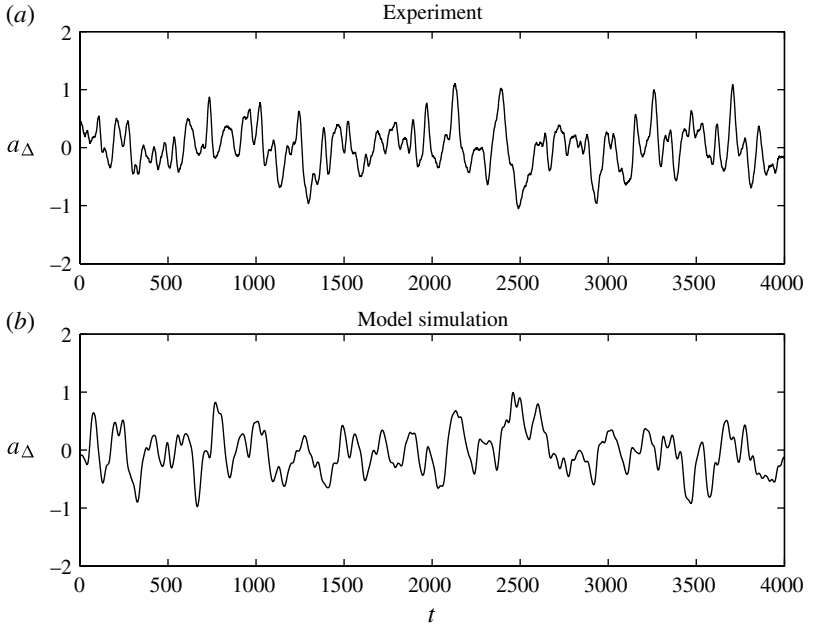


FIGURE 29. Evolution of the shift-mode amplitude a_Δ of (a) the experiment and (b) of the least order model (A 8).

https://doi.org/10.1017/jfm.2013.494 Published online by Cambridge University Press

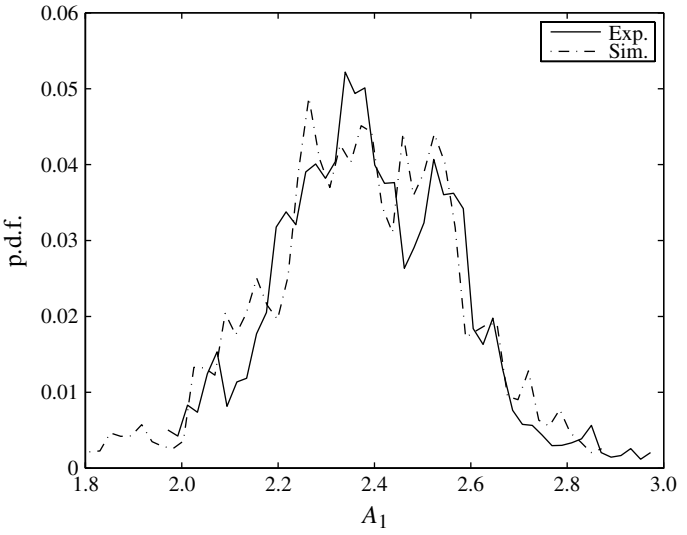


FIGURE 30. Probability density functions of the oscillation amplitude A_1 of the experiment (solid line) and of the least-order model (A 8) (dashed line).

simulation. A good agreement is achieved, particularly taking into account the simplicity of the stochastic model. It should be noted that the mode amplitudes of the constructed three-dimensional flow are based on Gaussian-filtered pressure signals. Hence, a fair comparison between experiment and model requires the same filtering to the model solution. This filtering of the model solution is performed in all mentioned figures. Otherwise, high-frequency noise of the Wiener process will become more apparent in the model solution.

Figures 30 and 31 display the p.d.f. of A_1 and a_Δ in experiment and simulation. The agreement can, again, be considered as good.

Finally, phase portraits of the model solution are depicted in figure 32. Not surprisingly, the model solution trajectory covers a similar area as the shown experimental data points.

In summary, the mode amplitudes of the three-dimensional velocity field is well reproduced by the least-order dynamical system (A 8). This indicates a surprising validity of laminar mean-field considerations even for turbulent wakes. These observations stimulate a detailed investigation of the underlying physics incorporating the Reynolds equation, Reynolds stress, etc. This investigation, however, exceeds the scope of this study which focuses on the flow kinematics from experimental data.

Appendix B. Procedure and CPU load

In this appendix, we summarize the procedural steps and computational load leading to the three-dimensional constructed flow and corresponding dynamical model.

Step 1: Filter of two-dimensional PIV data (x–y and x–z planes) The goal of this work package is the computation of the constitutive elements of the base flow, $\boldsymbol{u}_\Delta(\boldsymbol{x})$, $a_\Delta(t)$, of the first harmonics, $\boldsymbol{u}_1^a(\boldsymbol{x})$, $\boldsymbol{u}_2^a(\boldsymbol{x})$, $a_1^a(t) = A_1(t)\cos\phi_1(t)$, $a_2^a(t) = A_2(t)\sin\phi_1(t)$, and second harmonics in the respective plane.

(a) Extract the base flow contribution $\boldsymbol{u}_B(\boldsymbol{x}, t) = \boldsymbol{U}(\boldsymbol{x}) + a_\Delta(t)\boldsymbol{u}_\Delta(\boldsymbol{x})$. This implies: (i) computing the mean flow $\boldsymbol{U}(\boldsymbol{x}) = \overline{\boldsymbol{u}(\boldsymbol{x}, t)}$; (ii) applying a (low-pass) Gaussian filter to

https://doi.org/10.1017/jfm.2013.494 Published online by Cambridge University Press

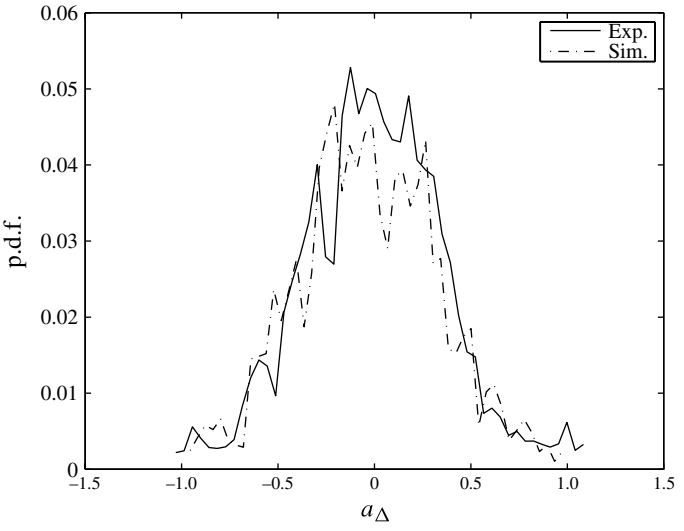


FIGURE 31. Probability density functions of the shift-mode amplitude a_Δ of the experiment (solid line) and of the least-order model (A 8) (dashed line).

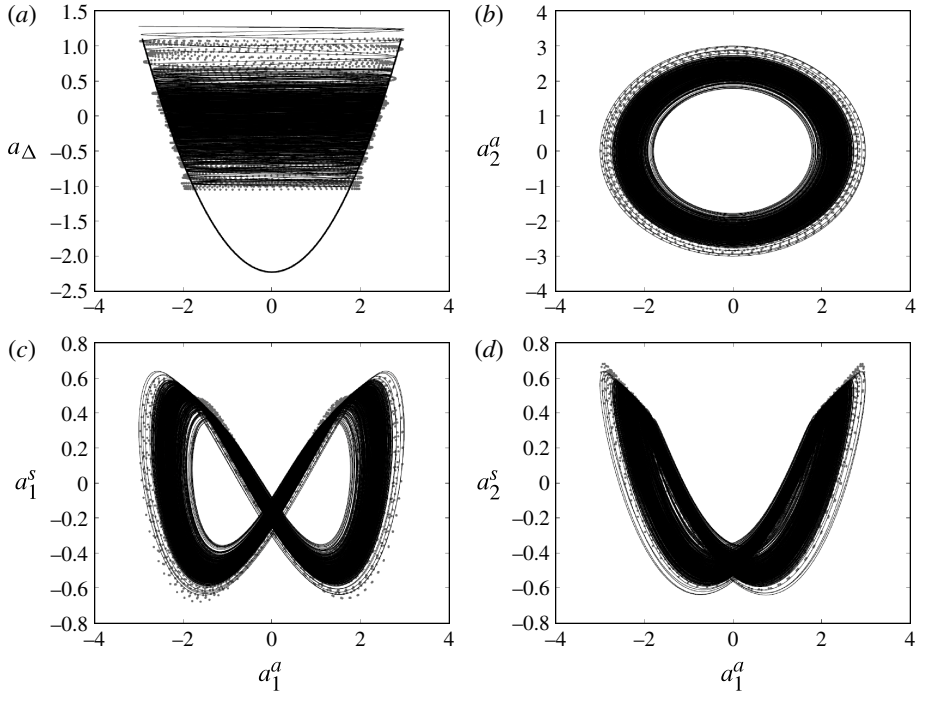


FIGURE 32. Same as figure 27, but for a filtered solution of the least-order model (A 8) (solid line). The amplitudes of corresponding experiment snapshots are marked as grey solid circles.

https://doi.org/10.1017/jfm.2013.494 Published online by Cambridge University Press

Time (s)	Task
553	POD of PIV data in the x–y plane with 5000 snapshots
337	POD of PIV data in the x–z plane with 5000 snapshots
83	Velocity pressure correlation (Step 2)
4840	Three-dimensional velocity field construction and POD
5813	Sum of all tasks

TABLE 2. CPU times of the most expensive tasks. The computations were performed on a laptop with 2 GB of RAM and an Intel Core i7 processor at 2.80 GHz. The times (in seconds) are wall times, i.e. include I/O, and could be optimized significantly.

time-resolved PIV data $\langle \boldsymbol{u}(\boldsymbol{x},t) - \boldsymbol{U}(\boldsymbol{x})\rangle_G$; (iii) performing a POD of the filtered data; and (iv) identifying the first POD mode and its amplitude with the shift mode $\boldsymbol{u}_\Delta$ and a_Δ, respectively.

(b) Extract the first harmonic as a periodic driving force $a_1^a(t)\boldsymbol{u}_1^a(\boldsymbol{x}) + a_2^a(t)\boldsymbol{u}_2^a(\boldsymbol{x})$, $a_1 + \imath a_2 = A_1 \exp[\imath\phi_1]$. This implies: (i) filtering out the antisymmetric velocity component $\boldsymbol{u}^a$ of the high-pass filtered velocity $\boldsymbol{u}'(\boldsymbol{x},t) = \boldsymbol{u}(\boldsymbol{x},t) - \boldsymbol{u}_B(\boldsymbol{x},t)$; (ii) performing a POD of this contribution; and (iii) identifying the first two POD modes $\boldsymbol{u}_i^a$, $i = 1, 2$, as the fields associated with $\cos\phi_1$ and $\sin\phi_1$, respectively.

(c) Extract the second harmonics. Repeat the previous step analogously with the symmetric component $\boldsymbol{u}^s$. See figure 4 and the corresponding text.

Step 2: Filter of pressure signals. Here, the pressure is filtered to derive analogue quantities of the shift-mode amplitude a_Δ, the amplitude A_1 and phase ϕ_1 of the velocity field. These quantities are the Gaussian-filtered symmetric pressure signal $\langle p^s\rangle_G$ and amplitude A_p and phase ϕ_p inferred from a complex Morlet-filtered antisymmetric signal.

Step 3: Correlation between pressure and velocity data. Here, the coefficients of (4.5) are determined from a standard least-squares approach.

Step 4: Construction of time-resolved three-dimensional flows.

(a) Take the time-resolved pressure signals as a synchronizing drive. This implies determining the three characteristic parameters of step 2.

(b) Compute for each pressure reading the most correlated velocity fields in all planes. See, e.g., figure 3 for the planes. The mapping from pressure to velocity field is defined in step 3.

(c) Interpolate the three-dimensional velocity field in a three-dimensional domain on a user-defined grid. The chosen equidistant Cartesian grid resolves the x, y and z coordinates with $75 \times 49 \times 31$ nodes. The trilinear interpolation technique is described in Press *et al.* (1986).

Step 5: Generalized phase average of three-dimensional flows. Proceed in complete analogy to Step 1, but for the three-dimensional constructed velocity field.

Step 6: Dynamical model for the modal amplitudes. See appendix A

All of the above steps can be conveniently performed on a conventional laptop, as shown in table 2.

REFERENCES

ADRIAN, R. & MOIN, P. 1988 Stochastic estimation of organized turbulent structure: homogeneous shear flow. *J. Fluid Mech.* **190**, 531–559.

BONNET, J.-P. (Ed.) 1998 *Eddy Structure Identification*. CISM Courses and Lectures, vol. 353. Springer.

https://doi.org/10.1017/jfm.2013.494 Published online by Cambridge University Press

BORÉE, J. 2003 Extended proper orthogonal decomposition: a tool to analyse correlated events in turbulent flows. *Exp. Fluids* **35**, 188–192.

BOURGEOIS, J. A., SATTARI, P. & MARTINUZZI, R. J. 2011 Alternating half-loop shedding in the turbulent wake of a finite surface-mounted square cylinder with a thin boundary layer. *Phys. Fluids* **23**, 095101.

DEANE, A. E., KEVREKIDIS, I. G., KARNIADAKIS, G. E. & ORSZAG, S. A. 1991 Low-dimensional models for complex geometry flows: application to grooved channels and circular cylinders. *Phys. Fluids* A **3**, 2337–2354.

DUŠEK, J., LE GAL, P. & FRAUNIÉ, P. 1994 A numerical and theoretical study of the first Hopf bifurcation in a cylinder wake. *J. Fluid Mech.* **264**, 59–80.

FARGE, M., SCHNEIDER, K., PELLEGRINO, G., WRAY, A. & ROGALLO, B. 2003 Coherent vortex extraction in three-dimensional homogeneous turbulence: comparison between CVS–wavelet and POD–Fourier decompositions. *Phys. Fluids* **15**, 2886–2896.

FLETCHER, C. A. J. 1984 *Computational Galerkin Methods*, 1st edn. Springer.

GLAUSER, M., EATON, E., TAYLOR, J., COLE, D., UKEILEY, L., CITRINI, J. H., GEORGE, W. K. & STOKES, S. 1999 Low-dimensional descriptions of turbulent flow: experiment and modelling. In *AIAA Fluids 1999 Conference and Exhibit. Norfolk, VA, USA, June 28–July 1, 1999*, AIAA paper 99-3699.

HALLER, G. 2001 Distinguished material surfaces and coherent structures in three-dimensional fluid flows. *Physica* D **149**, 248–277.

HALLER, G. 2005 An objective definition of a vortex. *J. Fluid Mech.* **525**, 1–26.

HOLMES, P., LUMLEY, J. L., BERKOOZ, G. & ROWLEY, C. W. 2012 *Turbulence, Coherent Structures, Dynamical Systems and Symmetry*, 2nd edn. Cambridge University Press.

HUNT, J. C. R., WRAY, A. A. & MOIN, P. 1988 Eddies, stream, and convergence zones in turbulent flows. *Tech. Rep.* CTR-S88. Center for Turbulence Research.

KASTEN, J., HOTZ, I., NOACK, B. R. & HEGE, H.-C. 2012*a* Vortex merge graphs in two-dimensional unsteady flow fields. In *Proceedings of the Joint EG/IEEE Symposium on Visualization (EuroVis 2012)*.

KASTEN, J., REININGHAUS, J., HOTZ, I., HEGE, H.-C., NOACK, B. R., DAVILLER, G., COMTE, P. & MORZYŃSKI, M. 2012*b* Acceleration feature points of unsteady shear flows. *SIAM J. Appl. Dyn. Syst.* (submitted).

LIU, J. T. C. 1989 Coherent structures in transitional and turbulent free shear flows. *Annu. Rev. Fluid Mech.* **21**, 285–315.

LUCHTENBURG, D. M., GÜNTER, B., NOACK, B. R., KING, R. & TADMOR, G. 2009 A generalized mean-field model of the natural and actuated flows around a high-lift configuration. *J. Fluid Mech.* **623**, 283–316.

LUGT, H. J. 1995 *Vortex Flow in Nature and Technology*, reprint edn. Krieger Publishing Company.

NOACK, B. R. 2006 Niederdimensionale Galerkin–Modelle für laminare und transitionelle freie Scherströmungen (translation: low-dimensional Galerkin models of laminar and transitional free shear flows). Habilitation thesis, Berlin Institute of Technology, Germany.

NOACK, B. R., AFANASIEV, K., MORZYŃSKI, M., TADMOR, G. & THIELE, F. 2003 A hierarchy of low-dimensional models for the transient and post-transient cylinder wake. *J. Fluid Mech.* **497**, 335–363.

NOACK, B. R., MORZYŃSKI, M. & TADMOR, G. (Eds) 2011 *Reduced-Order Modelling for Flow Control*. CISM Courses and Lectures, vol. 528. Springer.

NOACK, B. R., PAPAS, P. & MONKEWITZ, P. A. 2005 The need for a pressure-term representation in empirical Galerkin models of incompressible shear flows. *J. Fluid Mech.* **523**, 339–365.

NOACK, B. R., SCHLEGEL, M., MORZYŃSKI, M. & TADMOR, G. 2010 System reduction strategy for Galerkin models of fluid flows. *Intl J. Numer. Meth. Fluids* **63** (2), 231–248.

OBERLEITHNER, K., SIEBER, M., NAYERI, C. N., PASCHEREIT, C. O., PETZ, C., HEGE, H.-C., NOACK, B. R. & WYGNANSKI, I. 2011 Three-dimensional coherent structures in a swirling jet undergoing vortex breakdown: stability analysis and empirical mode construction. *J. Fluid Mech.* **679**, 383–414.

PERRIN, R., BRAZA, M., CID, E., CAZIN, S., MORADEI, F., BARTHET, A., SEVRAIN, A. & HOARAU, Y. 2006 Near-wake turbulence properties in the high Reynolds number

https://doi.org/10.1017/jfm.2013.494 Published online by Cambridge University Press

incompressible flow around a circular cylinder measured by two- and three-component PIV. *Flow Turbul. Combust.* **77**, 185–204.

PERRY, A. E. & CHONG, M. S. 1987 A description of eddying motions and flow patterns using critical-point concepts. *Annu. Rev. Fluid Mech.* **19**, 125–155.

PRESS, W. H., FLANNERY, B. P., TEUKOLSKY, S. A. & VETTERLING, W. T. 1986 *Numerical Recipes. The Art of Scientific Computing*. Cambridge University Press, Sec. 3.6, pp. 95–97.

REYNOLDS, W. C. & HUSSAIN, A. K. M. F. 1972 The mechanics of an organized wave in turbulent shear flow. Part 3. Theoretical models and comparisons with experiments. *J. Fluid Mech.* **54**, 263–288.

ROWLEY, C. W., MEZIĆ, I., BAGHERI, S., SCHLATTER, P. & HENNINGSON, D. S. 2009 Spectral analysis of nonlinear flows. *J. Fluid Mech.* **645**, 115–127.

ROWLEY, C. W. & WILLIAMS, D. R. 2006 Dynamics and control of high-Reynolds number flows over open cavities. *Annu. Rev. Fluid Mech.* **38**, 251–276.

SATTARI, P., BOURGEOIS, J. A. & MARTINUZZI, R. J. 2012 On the vortex dynamics in the wake of a finite surface-mounted square cylinder. *Exp. Fluids* **52** (5), 1149–1167.

SCHLEGEL, M., NOACK, B. R., JORDAN, P., DILLMANN, A., GRÖSCHEL, E., SCHRÖDER, W., WEI, M., FREUND, J. B., LEHMANN, O. & TADMOR, G. 2012 On least-order flow representations for aerodynamics and aeroacoustics. *J. Fluid Mech.* **697**, 367–398.

SCHMID, P. J. 2010 Dynamic mode decomposition for numerical and experimental data. *J. Fluid Mech.* **656**, 5–28.

TADMOR, G., LEHMANN, O., NOACK, B. R., CORDIER, L., DELVILLE, J., BONNET, J.-P. & MORZYŃSKI, M. 2011 Reduced-order models for closed-loop wake control. *Phil. Trans. R. Soc.* A **369**, 1513–1524.

TADMOR, G., LEHMANN, O., NOACK, B. R. & MORZYŃSKI, M. 2010 Mean field representation of the natural and actuated cylinder wake. *Phys. Fluids* **22**, 034102.

TAYLOR, J. A. & GLAUSER, M. N. 2004 Towards practical flow sensing and control via POD and LSE based low-dimensional tools. *Trans. ASME: J. Fluids Engng* **126**, 337–345.

WANG, H. & ZHOU, Y. 2009 The finite-length square cylinder near-wake. *J. Fluid Mech.* **638**, 453–490.

WANG, H., ZHOU, Y., CHAN, C. K. & LAM, K. 2006 Effect of initial conditions on interaction between a boundary layer and a wall-mounted finite-length-cylinder wake. *Phys. Fluids* **18**, 065106.

WESTERWEEL, J. 2000 Theoretical analysis of the measurement precision in particle image velocimetry. *Exp. Fluids* **29**, S3–S12.

WILLIAMSON, C. H. K. 1996 Vortex dynamics in the cylinder wake. *Annu. Rev. Fluid Mech.* **28**, 477–539.

https://doi.org/10.1017/jfm.2013.494 Published online by Cambridge University Press